https://doi.org/10.5194/wes-2026-114
Preprint. Discussion started: 28 July 2026

eawe european academy of wind energy
Open Access WIND ENERGY SCIENCE DISCUSSIONS

Dual-Doppler Radar Characterization during the Krummendeich Field Experiment: A Campaign Overview and Performance Assessment

Arianna Jordan[1], Lin-Ya Hung[1], Gerrit Wolken-Möhlmann[1], and Julia Gottschall[1,2]
[1]Fraunhofer Institute for Wind Energy System IWES, Bremen, Germany
[2]Faculty of Geosciences, University of Bremen, Bremen, Germany
Correspondence: Arianna Jordan (arianna.jordan@iwes.fraunhofer.de)

Abstract. The Krummendeich campaign in northern Germany was a field experiment designed to test dual-Doppler radar (DDR) technology for resolving flow fields. The campaign took place at the WiValdi research wind farm containing two operating turbines. Throughout the measurement period, a comprehensive observational network consisted of DDR, scanning and profiling lidars, a microwave radiometer, a meteorological mast, and laser disdrometers. Capitalizing on these datasets, the study herein offers an overview of the campaign while demonstrating the utility of the DDR method as a wind measurement tool for wind energy applications, specifically. This is done through validations against a co-located Doppler scanning lidar, assessments of data availability across meteorological conditions, and analyses of the method's capability to resolve flow features, i.e., turbine wake signatures. The site's temperate maritime climate, marked by frequent precipitation and wind direction-dependent stability regimes, provided a naturally diverse atmospheric environment for testing the method across conditions relevant to central European wind energy deployments. Validation showed great agreement with scanning lidar across most height levels, with discrepancies mainly occurring at near-surface levels. Hydrometeor presence strongly governed data availability, where precipitating periods sustained near-complete domain coverage. While radar returns were occasionally affected by artifacts even during otherwise well-covered scans, the method successfully captured both low-level jet and turbine wake within its flow field. Together, these results performance verification contribute to a continuously growing body of evidence supporting DDR as a viable and scalable tool for wind energy research and industry, with plans for deeper analysis and additional fieldwork to follow.

1 Introduction

Wind energy is expanding rapidly as a renewable energy resource worldwide, driving demand for accurate characterization of the effects from wind farms and the local environment surrounding them. Turbine wakes are observable in the flow field (e.g., Christiansen and Hasager, 2005; Platis et al., 2018; Gottschall, 2022), yet many properties associated with wakes (i.e., wake evolution) remain poorly understood with traditional observational capabilities. This gap in understanding grows increasing critical to address as wind farm installations continue to scale, so it is necessary to identify measurement methods capable of accurately measuring flow environments and turbine wake signatures within them. This need spans both the research com-

https://doi.org/10.5194/wes-2026-114
Preprint. Discussion started: 28 July 2026

Open Access
WIND ENERGY SCIENCE DISCUSSIONS

munity, where high-quality observations underpin field campaign design and model development, and industry, where such measurements inform wind farm layout decisions and energy yield estimates.

Existing approaches for wind measurement are plentiful, but each carries known limitations. Meteorological masts have long been an industry standard for in-situ wind measurement, but their data are typically confined to near-surface levels and leave gaps in coverage around turbine and boundary layer heights. Synthetic aperture radar (SAR) satellite retrievals have been used effectively to observe elongated wakes (Christiansen and Hasager, 2005; Li et al., 2014; Hasager et al., 2015; Ahsbahs et al., 2020), but are subject to infrequent revisit times and limited vertical information. Airborne measurements have been successfully employed for limited deployment periods (Emeis et al., 2016; Platis et al., 2018; Lampert et al., 2026), yet such platforms are costly and unsuitable for sustained, long-term observing. To date, Doppler wind lidars has been continuously used as a reliable resource for providing robust wake observations (e.g., Bingöl et al., 2010; Trujillo et al., 2011; Iungo et al., 2013; Clifton et al., 2018; Gottschall et al., 2021; Patel et al., 2025) due to their easy mobility and ample vertical coverage paired with high-resolution profiling. Vertical profiling lidars can supply low-level wind data encompassing turbine heights while Doppler scanning lidar can extend throughout the atmospheric boundary layer. However, both are constrained by a spatial range that is often insufficient for resolving the full extent of wake evolution at the farm scale.

A dual-Doppler radar (DDR) setup, in which two radars sample the same scanning volume, is a well-established meteorological technique that has recently gained attention for wind energy applications. By combining radial velocity measurements from two spatially-separated radar units, DDR retrieves two-dimensional wind vector fields over large horizontal areas under a rapid return times. This allows observation of the spatial extent and evolution of turbine wakes, while radar scans collected at multiple heights can be stacked to visualize vertical wake structure as is commonly examined with lidars. The DDR method has a well-established history in mesoscale and convective meteorology (Lhermitte and Gilet, 1975; Bluestein et al., 2014), where precipitation events yield the most data-rich returns, but its application in the context of wind energy is relatively novel. Early demonstrations confirmed its utility for documenting single-turbine wakes and wind ramp events (Hirth and Schroeder, 2013), and subsequent offshore deployments revealed wake structures extending well beyond the measurement domain (Nygaard and Newcombe, 2018).

More recently, the 2022–2024 American WAKE experimeNt (e.g; Moriarty et al., 2020, 2024) was a large-scale field campaign in northern Oklahoma, U.S. in which two X-band radars in a DDR setup were deployed. During that time, the radars were configured to measure high-quality wind fields across a large domain encompassing multiple wind farms. Findings from AWAKEN offered new and important insights into the capabilities of DDRs compared to lidar platforms. Hung et al. (2024) verified the X-band radar's line-of-sight wind speed against a co-located scanning lidar at 2 km range, finding strong overall agreement (R^2 = 0.989). Vöhringer et al. (2024) compared DDR-reconstructed wind speed and direction with profiling lidars and found generally good agreement, particularly for lidars located closest to the radars. However, the radar systematically overestimated wind speed near the surface, which they attributed to inhomogeneous wind fields that are sampled differently by the lidar and DDR due to their differing measurement volumes and strategies. Abraham et al. (2024) reported a similar low-level positive bias in scanning lidar–DDR comparisons within the lowest 150 m, but attributed this to grid interpolation effects arising from the removal of ground clutter. There are also ongoing developments in filtering techniques to explore for

https://doi.org/10.5194/wes-2026-114
Preprint. Discussion started: 28 July 2026

eawe european academy of wind energy
Open Access WIND ENERGY SCIENCE DISCUSSIONS

improving DDR based wind retrievals (e.g; Zheng et al., 2026). These studies provide important considerations for DDR under the scanning strategy implemented during AWAKEN, however, those settings sought a large spatial domain where uncertainties can be amplified compared to smaller-scale deployments. It is worth exploring DDR performance in more confined setting where limitations associated with the complementary DDR configuration are easier to characterize if not eliminated completely. Moreover, how DDR performance varies with the prevailing atmospheric regime is necessary, especially in environments that differ from Oklahoma's semi-arid climate.

The 2025 Krummendeich field experiment in northern Germany provided an ideal testbed to address this gap. This onshore campaign took place near a small number of operating turbines to target a fine-scale, turbulence-relevant evaluation of DDR winds. The site was heavily instrumented, including two temporary X-band radars for DDR analysis, a meteorological mast, scanning lidars, a vertical profiling lidar, laser disdrometers, and additional supporting measurements. All instruments were deployed within a relatively compact domain (<10 km in all directions), providing a more controlled spatial setting compared than employed during AWAKEN. The breadth of collocated observations enables a comprehensive characterization of atmospheric conditions during the campaign, including their representativeness relative to the regional climatology. Furthermore, by leveraging co-located scanning lidar observations with well-established performance and uncertainty characteristics in wind energy applications, the Krummendeich campaign allows a systematic validation and performance evaluation of DDR-derived winds across a range of atmospheric conditions. Such information is necessary to expand knowledge into the applicability of DDR in wind energy applications, including field campaigns, numerical modeling, and industry use.

This study explores DDR as a tool for observing high-quality wind flow, waked or otherwise, using the observation-rich, small-scale Krummendeich campaign. In alignment with the objectives of the Windpark-RADAR project, the focus is placed on identifying both the capabilities and limitations of DDR in northern Germany's temperate maritime environment. By emphasizing condition-dependent performance rather than case-specific demonstration, this work contributes to defining when DDR retrievals are reliable and supports the development of strategies for its operational deployment in the wind energy industry. This manuscript consists of methods describing the site and campaign (Chapter 2). Next, results are presented of atmospheric conditions during the campaign, validations between the DDR and scanning lidar, DDR performance during different sky conditions, and the ability of DDR to resolve features in the flow field (Chapter 3), a discussion of the findings (Chapter 4), and, lastly, the conclusions (Chapter 5).

2 Methods

2.1 Site Design and Meteorological Conditions

The Krummendeich field campaign was carried out at the WiValdi Wind Park, a research facility operated by the German Aerospace Center (DLR) in Krummendeich, Germany (Figure 1). The site is situated on low-lying flatlands near the mouth of the River Elbe estuary, approximately 40 km from the North Sea. This research facility contains two 4.2 MW Enercon E-115 wind turbines (hub heights = 92 m; rotor diameters = 116 m) (Wildmann et al., 2024). The surrounding terrain is

https://doi.org/10.5194/wes-2026-114
Preprint. Discussion started: 28 July 2026

eawe european academy of wind energy
Open Access WIND ENERGY SCIENCE DISCUSSIONS

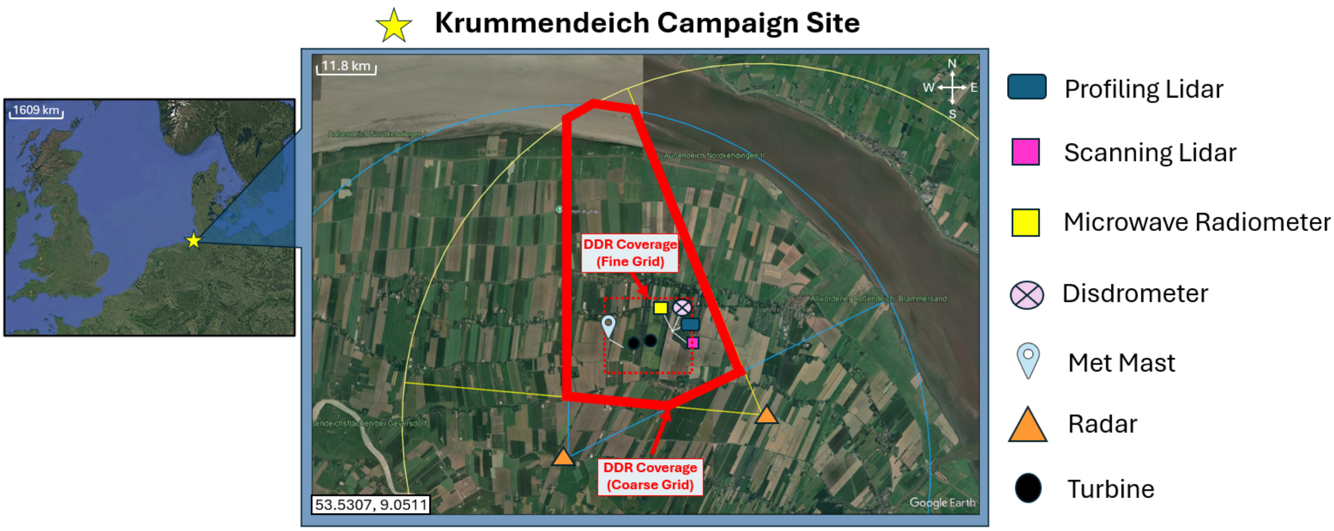

Figure 1. Bird's eye view of the northern Germany and surrounding area (top left) with a zoomed-in version of the Krummendeich campaign domain (right). Pin-marked locations represent the instruments referenced in this work: the profiling lidar, the scanning lidar, the microwave radiometer, the disdrometers, the met mast, the two X-band radars, and the operating turbines. Image © 2025 Google Earth Pro; imagery data from Landsat/Copernicus Map backgrounds: © 2026 Maxar Technologies, © 2026 Airbus; Image Landsat/Copernicus. Source: Google Earth Pro

topographically simple, with minimal orographic complexity, making it well suited for investigating instrument capabilities that terrain-induced flow could otherwise distort.

In terms of climatology, the WiValdi research facility is located within a temperate maritime environment as part of the North German lowlands. Cloud cover and frequent precipitation is common year-round, driven by the passage of mid-latitude cyclones. These synoptic systems are the primary source of rainfall at the site, delivering frontal precipitation that can persist for extended periods and is associated with strong southwesterly to westerly winds ahead of cold fronts. This behavior has been attributed to the large-scale low-pressure systems in the Northern Hemisphere, which drive cold-sector northwesterly flow over the warmer sea surface and warm-sector southwesterly flow over cooler land at night (Emeis et al., 2016). Though the site is not too far from the North Sea, it is inland enough that an oceanic influence is reduced. As such, a humid continental climate, with warm summers, cold and rainy winters, and more pronounced seasonal temperature variations can be expected (Peel et al., 2007; Zhou et al., 2025).

One unique facet of the WiValdi location is the range of atmospheric stability regimes that are strongly governed by wind direction. As observed by Emeis et al. (2016) and Wildmann et al. (2022), winds from the northwest originate over the relatively warm North Sea surface and tend to be associated with convectively unstable or near-neutral conditions, whereas winds from the southeast arrive over the relatively cool land surface at night and are more frequently stably stratified. The latter study showed winds overall to be most common from the southwest. Another feature to consider are low-level jets (LLJs), which are

https://doi.org/10.5194/wes-2026-114
Preprint. Discussion started: 28 July 2026

eawe european academy of wind energy
Open Access WIND ENERGY SCIENCE DISCUSSIONS

also a prominent feature of the nocturnal boundary layer at this site. Wildmann et al. (2022) found LLJs to be present on 49% of nights at Krummendeich, reflecting the site's exposure to stable nocturnal drainage flows and the strong surface cooling that occurs over the flat coastal terrain under clear skies. These LLJ events are also of particular relevance to wind energy, as they can produce pronounced wind shear at rotor-level heights and are worth considering in the present study.

2.2 Campaign and Instrument Specifics

The full duration of the Krummendeich field experiment ran from 19 March 2025–9 January 2025, which is the period assessed when exploring general atmospheric conditions throughout the campaign. The first official DDR data collections began on 5 June 2025, and the DDR-lidar comparisons focused from then to just before the relocation of the scanning lidar on 6 September 2025. An overview of availability from all instruments focused upon in this manuscript can be found in Figure 2. The DDR availability with height is shown in Table 1 across the coarse and fine grid domains.

The DDR measurements came from two X-band dual-Doppler radar units: Radar West (IWES-X2) and Radar East (IWES-X1). They were deployed approximately 5.3 km apart along a shared east–west baseline (9.195°E, 53.788°N and 9.274°E, 53.788°N, respectively), with both units mounted at approximately 7.7 m above ground level. Each radar performed 60° sector volumetric scans across up to 14 elevation angles, enabling three-dimensional wind field retrieval over the WiValdi research wind farm and extending to the neighboring Oederquart and Kajendeich turbine sites. The east–west baseline geometry was oriented to maximize dual-Doppler coverage of the predominant west-southwesterly inflow and the downstream wake region. While the DDR settings during AWAKEN prioritized wide 145° sectors at low elevation angles over a large domain of around 30 km, the DDR during the Krummendeich campaign performed narrower 60° sector scans of up to 9 km to favor vertical wind fields over a more localized domain. There were conventional and novel hard-targeting tests performed to confirm the position and pointing accuracy of the radar beams, which depicted a minor angular bias from the radars but no elevation bias (Hung and Gottschall, 2026).

In the measurement data, singularities with increased wind speeds and elevated backscatter values influenced the average wind speeds. Since these singularities moved over time, one-time measurement errors could be ruled out. The cause of this problem was identified as insects or groups of insects. Based on this knowledge, we developed and applied filters and adjusted processing to remove the distorted radial velocities. These radial velocity measurements from both radars were then processed onto two Cartesian grids: a coarse grid which spans the full measurement domain, and a fine grid, which yields higher resolution but a smaller domain, as seen in Figure 1 (note that this is implemented as a black-box processing with the full details not accessible to the authors). Next, the gridded fields underwent Dual-Doppler synthesis (Hirth and Schroeder, 2013) to reconstruct horizontal wind velocity vectors from the combined radial velocities of both radars (Given and Ray, 1994). We also considered the coverage factor of the radar scans, which is defined as the ratio of the number of bins that pass the filter to the number of available data bins. Available data bins are those in which the sampling volumes of both radars intersect; regions observed by only one radar are not included. For convenience, the coverage factor is reported as an integer flag from 0 to 9, corresponding to 0–100% coverage in steps of 10%. Here, only scans with a coverage factor of 8 or greater are considered, which is the value used during site acceptance tests. The primary scan pattern of the DDR was plan-position indicator (PPI)

https://doi.org/10.5194/wes-2026-114
Preprint. Discussion started: 28 July 2026

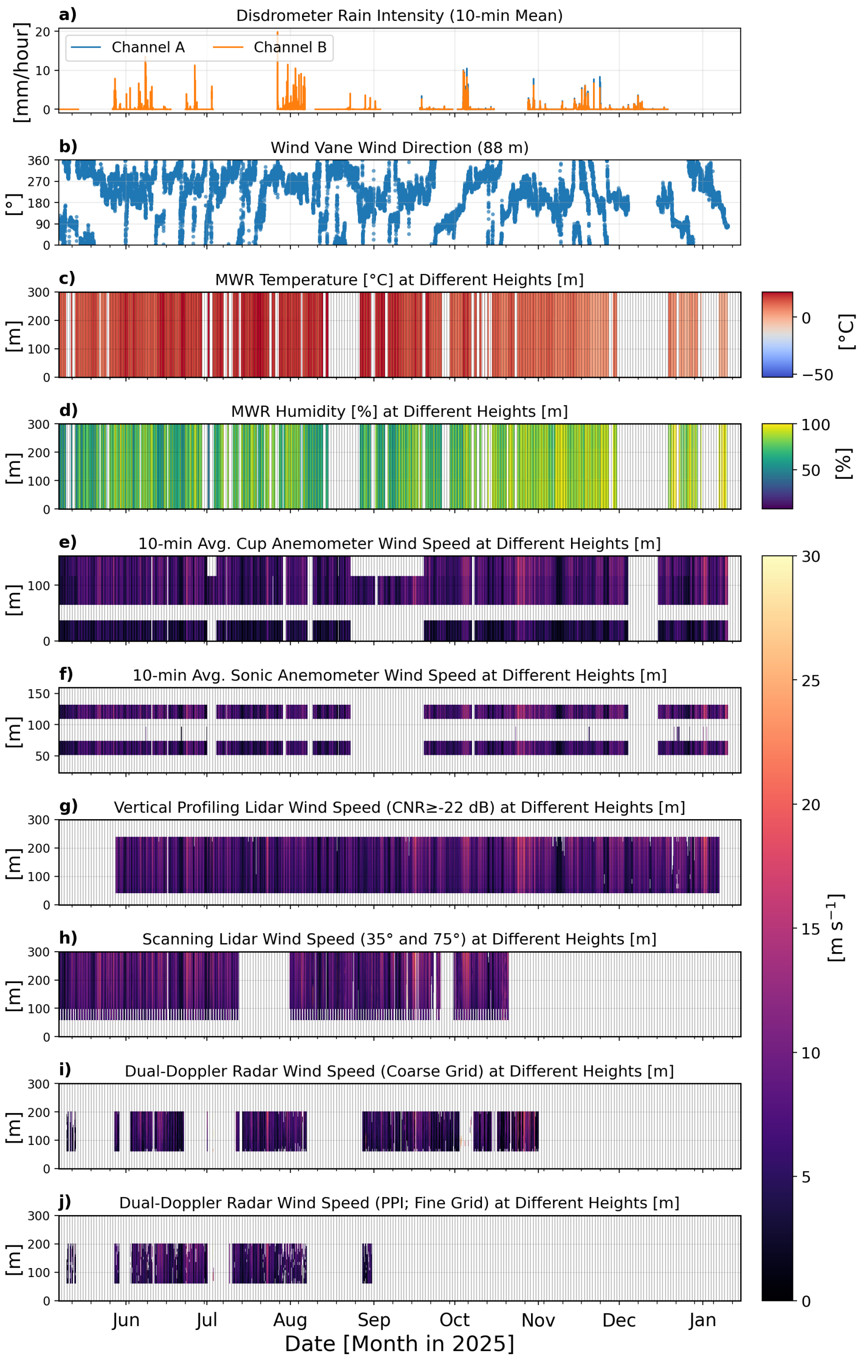

Figure 2. Data availability figure of all Krummendeich campaign instruments considered in this work. Panels a-j, respectively, show rain intensity as measured by the disdrometer, wind vane flow direction at 88 m, MWR temperature and humidity, and wind speed from the cup and sonic anemometer measurements, lidars, and DDR (both coarse and fine grid). The DDR scans were derived from a single grid point encompassing the location of the scanning lidar.

https://doi.org/10.5194/wes-2026-114
Preprint. Discussion started: 28 July 2026

Table 1. DDR coarse and fine grid availability of PPI scans with height. Percentages indicate the coverage out of the full spatial domain for the respective grid.

	Coarse grid		Fine grid	
Height [m]	**All data [%]**	**Coverage factor≥8 [%]**	**All data [%]**	**Coverage factor≥8 [%]**
60	9.40	10.29	66.53	75.11
70	12.39	13.71	66.26	75.20
80	14.15	15.86	65.55	75.05
90	15.20	17.26	64.92	75.07
100	15.63	17.94	64.43	75.29
110	15.64	18.08	64.19	75.71
120	15.50	18.03	64.02	76.17
130	15.19	17.79	63.87	76.58
140	14.76	17.41	63.63	76.88
150	14.21	16.91	63.18	76.94
160	13.56	16.27	61.87	75.99
170	12.86	15.57	59.38	73.50
180	12.17	14.84	56.04	69.76
190	11.46	14.06	51.71	64.69
200	10.80	13.33	46.57	58.53
210	10.17	12.62		
220	9.56	11.93		
230	8.97	11.26		
240	8.40	10.61		
250	7.87	10.00		
260	7.36	9.39		
270	6.89	8.84		
280	6.45	8.31		
290	6.02	7.78		
300	5.62	7.29		

scans. While the DDR also collected range-height indicator virtual tower scans after 14 November 2025, we focus only on its post-processed PPIs, a metric that is more favorable for comparisons with the scanning lidar.

Many supplementary instruments to the radars make up the Krummendeich campaign. The WiValdi site provides a met mast (DLR; 9.219°E, 53.814°N) and microwave radiometer (MWR; 9.219°E, 53.814°N) continuously operated by DLR. A vertical profiling lidar (9.238°E, 53.819°N; 4.7 m AGL) was stationed on top of the WiValdi control center. Co-located with the vertical profiling lidar (9.238°E, 53.819°N; 4.7 m AGL) were a pair of laser disdrometers (PA2-452494 and PA2-452495)

https://doi.org/10.5194/wes-2026-114
Preprint. Discussion started: 28 July 2026

eawe european academy of wind energy
Open Access WIND ENERGY SCIENCE DISCUSSIONS

provided by the Fraunhofer Institute for Wind Energy Systems (IWES), which record precipitation-related quantities continuously throughout the campaign. The disdrometers provide in situ measurements of precipitation intensity and raindrop size distribution, directly linking DDR data availability to the precipitation environment.

Finally, the lidar of interest for DDR-lidar comparisons is a WLS200S-217 scanning lidar (9.238°E, 53.819°N), which also came from IWES. Its scans cycled between 35° VADs intended for turbulence kinetic energy considerations and 75° VAD scans to favor tall wind profiling every 30 minutes, with a brief fixed vertical stare of approximately one minute performed between each alternation. The VAD range of accessible data was from 100-3825 m, with a range gate lengths of 50 m. More information on the operating specifics of this lidar and the other aforementioned instruments can be found in Table 2. This scanning lidar was selected as the DDR reference given its capabilities to scan well into the boundary layer, whereas observations from vertical profiling lidars are limited to the first few hundred meters. Throughout the Krummendeich campaign, this lidar and other instruments were cross-validated to assess how each captured the flow, including comparisons between met mast and the vertical profiling lidar; see Appendix Figure A1 for the profiling-scanning lidar comparisons, where multiple levels could be compared, which produced overall sensible agreement.

Table 2. Instrumentation and measurement parameters during the campaign. Note that here, standalone time units are abbreviated from seconds to sec, minutes to min. etc.

Instrument	Type / Model	Parameter	Height(s) / Range [m]	Unit	Resolution / Notes
Vertical Profiling Lidar	WindCube WLS7-277	Wind speed	40, 58, 88, 90, 103, 118,	m/s	10 min. horizontal wind speed
		Wind direction	133, 148, 168, 188, 213, 238	°	10 min. horizontal wind direction
Disdrometer Met System	Laser disdrometer (PA2-452494/495)	Precipitation	–	mm/60 sec.	10 min. & 30 sec.
	Airmar WX200 (S/N 60775290)	Sanity check for weather	–	–	–
Microwave Radiometer	HATPRO	Temperature	94 levels, 0–10,000 m (10–300 m spacing)	°C	10 min. & 30 sec.
	HATPRO	Humidity	94 levels, 0–10,000 m (10–300 m spacing)	%	–
WiValdi Met Mast	Sonic Anemometer	u, v, w, wind direction	Sonic-1: 149, 120, 61	m/s, Radians	uSonic 3 MP 3D; ±1% at 5 m/s
			Sonic-2: 120, 85, 62	m/s, Radians	resolution 0.006 m/s (vertical), 0.01 m/s (horizontal)
			Sonic-3: 120, 62, 33	m/s, Radians	
	Cup anemometer	Wind speed	Cup 1: 142, 90, 10	m/s	
			Cup 2: 143, 91, 33, 10	m/s	±1 of measured value or $< \pm 0.2$ m/s at 0.3–50 m/s
			Cup 3: 143, 91, 10	m/s	resolution 0.05 m wind path
	Wind vane	Wind direction	Vane-1: 87	Radians	
			Vane-2: 88	Radians	accuracy 1°,
			Vane-3: 88	Radians	resolution 0.35°
	Precipitation sensor	Precipitation	–	mm/60 sec.	
Scanning lidar WLS200S-217 (Zonda)	Scanning lidar	VAD75 (wind profile)	100–3825 (50 m gates)	m/s	Elevation: 75°, azimuth: 0–360°, accumulation time = 0.4 (sec.), 72 sec./scan, 25 iterations, ∼30 min; starts at full hour
		VAD35 (turbulent kinetic energy)	100–3825 (50 m gates)	m/s	Elevation: 35.3°, azimuth: 0–360°, accumulation time = 0.4 (sec.), 72 sec./scan, 25 iterations, ∼30 min.; starts at half hour
		Fixed vertical stare	100–3080 (50 m gates)	m/s	Elevation: 90°, azimuth: 0°, accumulation time = 0.2 sec., 0.2 sec./scan, loop (∼1 min.); in between VAD scans

https://doi.org/10.5194/wes-2026-114
Preprint. Discussion started: 28 July 2026

3 Results

3.1 Campaign vs. Climatology Conditions

To contextualize DDR performance throughout the campaign, we first characterize the atmospheric conditions observed at Krummendeich and assess their representativeness relative to the regional climatology. Doing so provides the foundation for interpreting condition-dependent instrument behavior in the results to follow. Winds during the campaign generally aligned with the climatological average of predominantly southwesterly flow (Figure 3), although there was a distinct difference between seasons. The warmer months exhibited an increased frequency of northwesterly flow, indicative of more frequent low-pressure passages (Wildmann et al., 2022).

In general, mid-latitude low pressure systems are common off the North Sea. Examples of their occurrence can be seen in Figure 4, which denote these systems in snapshots of synoptic conditions occurring during the three stability regimes (archives available from the Met Office UK). In contrast, the colder months were characterized by a return to predominantly southwesterly winds, consistent with the regional climatology. It should be noted that the winter of 2025 featured unusually frequent snowfall events in northern Germany, associated with episodic Arctic air intrusions. However, these events occurred within the prevailing westerly flow regime rather than reflecting a sustained shift in the dominant wind direction.

We estimated atmospheric stability at Krummendeich using the bulk Richardson number (Louis, 1979), as seen in Figure 5. This method incorporates both the thermodynamic stratification and the kinematic wind shear profile, making it a more physically complete stability metric than the simple temperature gradient lapse rate method. Although a MWR lapse rate

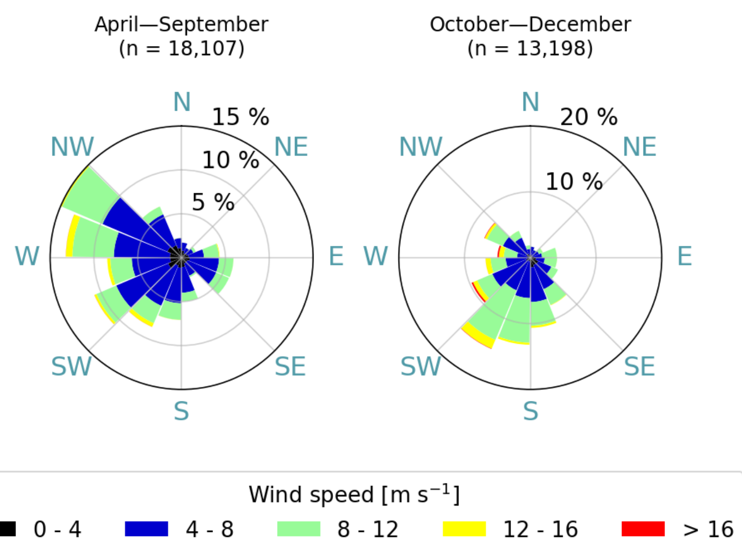

Figure 3. Wind roses from the vertical profiling lidar data near hub-height (90 m). The left panel represents the typical warm season (selected as 3 April - 30 September 2025) and the right depicts the typical cool season (selected as 1 October - 31 December 2025).

https://doi.org/10.5194/wes-2026-114
Preprint. Discussion started: 28 July 2026

approach produced broadly similar stability classifications over the campaign period (not shown), the bulk Richardson number is preferred here given its sensitivity to the dynamical suppression of turbulence by wind shear, which is particularly relevant in the coastal boundary layer environment of Krummendeich where strong shear frequently accompanies stably stratified flow. Figure 5a shows the diurnal cycle of stability class frequency over the full campaign. Stable conditions (dark blue) dominate the nighttime and early morning hours from approximately 20:00 to 05:00 UTC, while unstable conditions (yellow) emerge rapidly after sunrise and peak during the mid-morning to early afternoon hours between roughly 07:00 and 15:00 UTC. Neutral conditions (green) are present throughout the day but are most prominent during the morning and evening transition periods. This diurnal structure is consistent with the canonical pattern expected at a low-lying coastal site of Krummendeich.

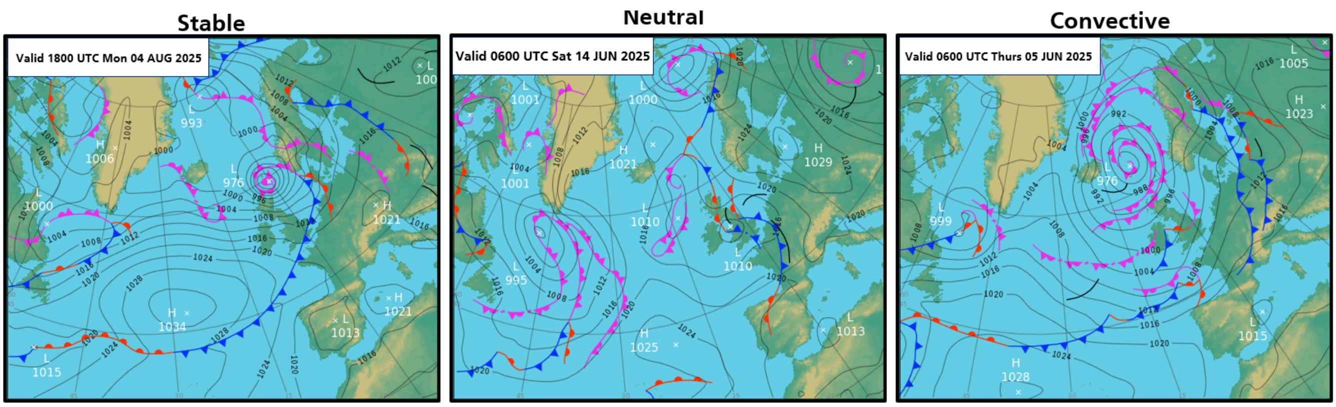

Figure 4. Three snapshots of stability regimes relevant for Krummendeich site characterization as captured by synoptic scale conditions. These maps are available from the Met Office UK at https://digital.nmla.metoffice.gov.uk/.

https://doi.org/10.5194/wes-2026-114
Preprint. Discussion started: 28 July 2026

eawe european academy of wind energy
Open Access WIND ENERGY SCIENCE DISCUSSIONS

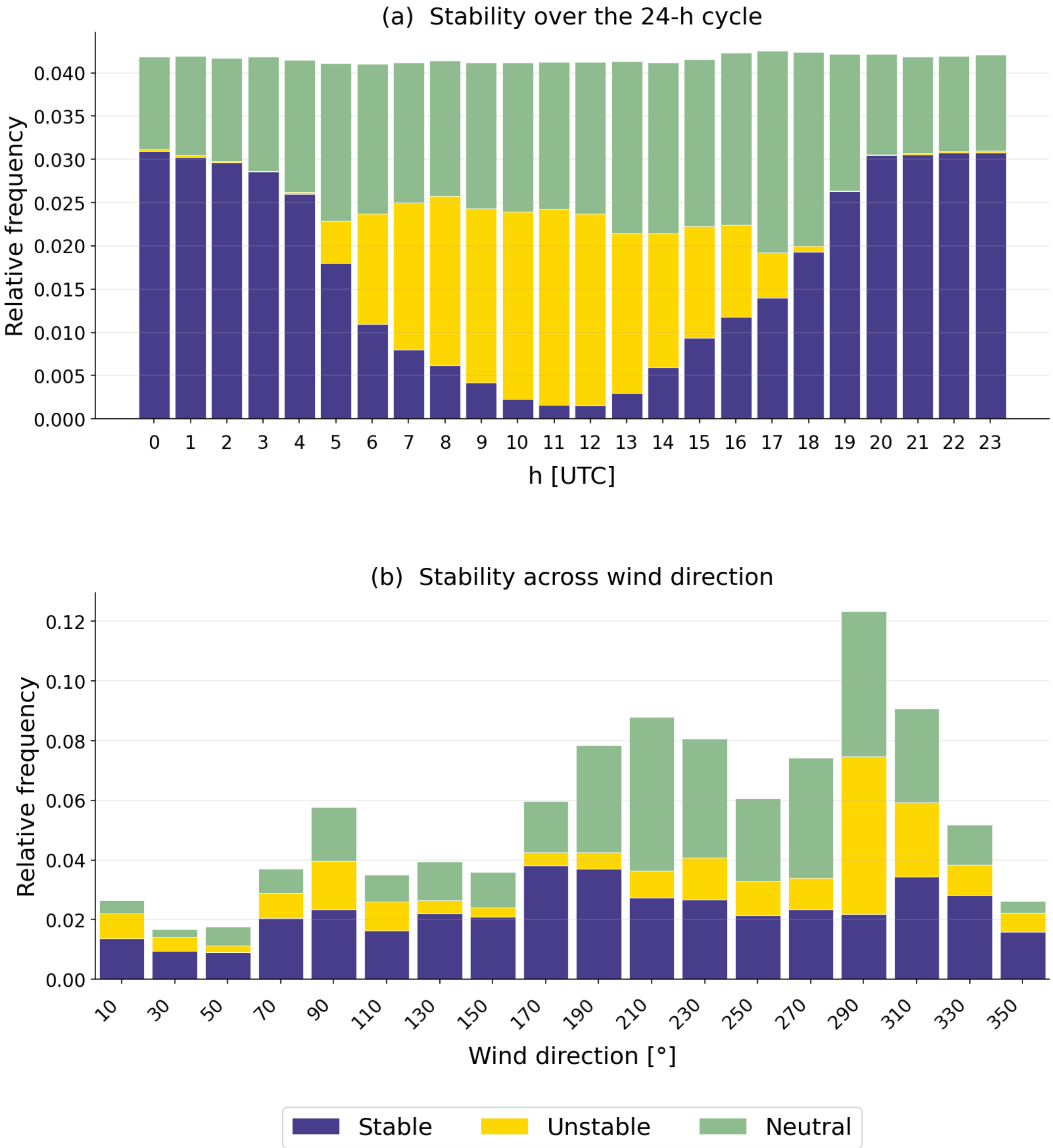

Figure 5. Atmospheric stability conditions as computed via the Bulk Richardson method from met mast data during 3 April-31 December 2025. Panel a depicts the stability as a function of time throughout the 24-hour cycle, and panel b shows the stability as a function of wind direction.

Figure 5b illustrates the distribution of stability classes as a function of wind direction. As in the wind roses, the prevailing wind directions are clearly westerly to northwesterly, with the 290–310° sector accounting for the largest share of observations. Winds from the northwest and west are predominantly neutral to unstable, while winds from the east and southeast (90–150°) show a comparatively higher proportion of stable conditions relative to their total frequency, consistent with seaward flow over

https://doi.org/10.5194/wes-2026-114
Preprint. Discussion started: 28 July 2026

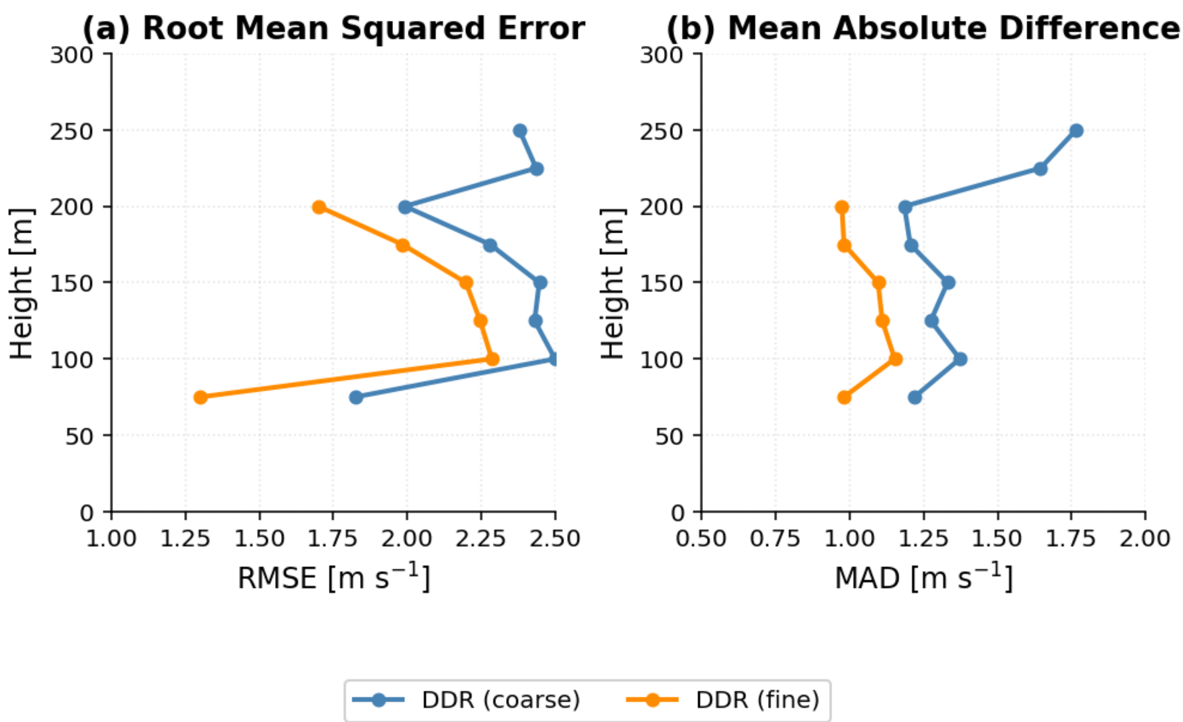

Figure 6. The root mean squared error (RMSE) and mean absolute deviation (MAD). Both were calculated by corresponding scanning lidar to DDR coarse grid and fine grid measurements.

the cooler land surface at night. This dependence of stability on wind direction aligns closely with the climatological patterns documented at this site by Platis et al. (2022) and Wildmann et al. (2022), supporting that the campaign period is broadly representative of the site's typical atmospheric behavior.

3.2 DDR-Scanning Lidar Validation

With the campaign's atmospheric conditions established as broadly representative of the regional climatology, we turn to a quantitative assessment of DDR wind retrieval performance. Validation against the co-located scanning lidar over the period 3 April to 6 September 2025 provides the primary benchmark, with datasets filtered to retain only timestamps common to both instruments at height levels agreeing to within 3 m and periods of heavy precipitation linked to erroneous or depleted lidar returns excluded.

Figure 6 presents vertical profiles of the root mean squared error (RMSE) and mean absolute difference (MAD) between scanning lidar wind speeds and retrievals from the fine and coarse grid configuration. This allowed an assessment into how the two DDR grids compare. Across all height levels, the fine grid consistently exhibited lower errors than the coarse grid in both metrics. The coarse grid showed more pronounced height-dependent variability, with errors increasing notably above 150

https://doi.org/10.5194/wes-2026-114
Preprint. Discussion started: 28 July 2026

eawe european academy of wind energy
Open Access WIND ENERGY SCIENCE DISCUSSIONS

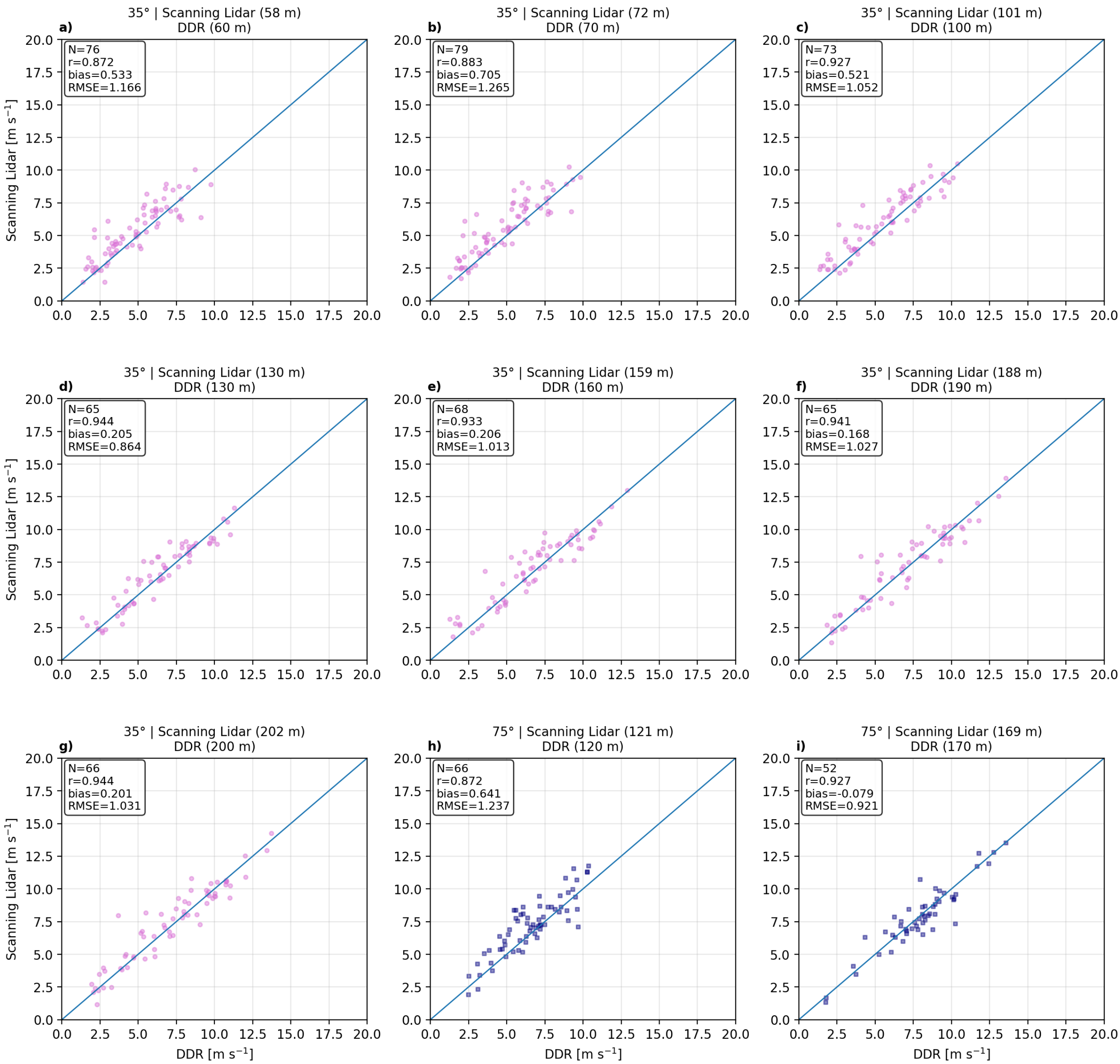

Figure 7. Scatterplots of horizontal wind speed retrieved from the DDR from 2025-04-03 to 2025-09-06. The 35° lidar scan is shown in panels a–g, and the 75° VAD scan is shown in panels h–i. Each panel reports the number of matched samples (N), Pearson correlation coefficient (r), mean bias (bias), and root mean square error (RMSE). Note that DDR retrieval heights are indicated in the panel title; scanning lidar heights are given in parentheses.

https://doi.org/10.5194/wes-2026-114
Preprint. Discussion started: 28 July 2026

eawe european academy of wind energy
Open Access WIND ENERGY SCIENCE DISCUSSIONS

m, which reflects the reduced spatial sampling density becoming more consequential as horizontal wind gradients grow with height. The superior performance of the fine grid is expected: its denser spatial sampling better resolves the wind field in the vicinity of the scanning lidar measurement volume, reducing the representativeness error inherent in comparing point-like lidar observations against spatially interpolated radar retrievals. With the fine grid confirmed as the higher-performing configuration, Figure 7 presents the full scatterplot validation results across all available height levels.

Despite the excess filtering leaving a relatively limited number of matched samples, wind speeds from the DDR and scanning lidar were in generally good agreement across the majority of height levels, with correlation coefficients ranging from 0.87 to 0.94 and RMSE values below 1.3 $\mathrm{m\,s^{-1}}$ for most comparisons. Agreement improved notably with height for the 35° lidar scans, with the weakest performance occurring at the two lowest levels (58 m and 72 m; Figs. 7a-b). This degradation is likely attributable to the geometry of the DDR retrievals: the lowest usable retrieval levels of the DDR are subject to a beam blind zone near the surface, reducing the accuracy of the reconstructed horizontal wind vector. At the 75° lidar elevation (Figs. 7h-i), elevated scatter is observed relative to the 35° comparisons at equivalent heights. Importantly, comparable scatter is also present when the scanning lidar's 75° retrievals are compared against the independent profiling lidar (Fig. A1g-h), suggesting that this degradation is an inherent limitation of the scanning lidar at this elevation angle rather than a deficiency in the DDR retrieval. At steep elevation angles, the radial velocity measured by the scanning lidar becomes increasingly sensitive to the vertical wind component, which the VAD retrieval assumes to be negligible. Violations of this assumption introduce additional uncertainty into the retrieved horizontal wind speed, explaining the consistently elevated scatter across both comparisons at 75°.

3.3 DDR Performance Under Different Atmospheric Conditions

The overall validation results establish that DDR wind retrievals compare well against scanning lidar across the campaign period, but aggregate statistics alone may obscure condition-dependent behavior. It was therefore useful to examine whether DDR performance varies systematically with depending on different atmospheric regimes. For instance, Figure 8 depicts wind speed and wind direction with height from the scanning lidar, the DDR coarse grid, and the DDR fine grid under stable (Fig. 8a-b), neutral (Fig. 8c-d), and unstable (Fig. 8e-f) conditions. Here, each wind speed bin is shown to range between 0-17 m s^{-1}, but the wind direction range varied across stability regime such as in Figure 5b. The DDR grid points nearest to the scanning lidar were used; note that their volumetric scans do not represent true vertical profiles. Timestamp matching was increased to 1 minute between the lidar and radar for a larger sample size; nevertheless, the same pattern for the few exact timestamp matches is seen here.

As a whole, the three measurement approaches showed excellent agreement regardless of atmospheric stability, with wind speeds well-matched across all conditions. The coarse grid showed slightly more underestimation than the fine grid, with the greatest deviation occurring in convective wind directions when flow is expected to be more inhomogeneous. A recurring trend in the fine grid was a slight overestimation of wind speeds relative to the lidar measurements under stable and convective conditions. Such findings are consistent with AWAKEN results from with Abraham et al. (2024) and Vöhringer et al. (2024), but the differences here were not as drastic. Comparably large values to those studies were originally observed even with

https://doi.org/10.5194/wes-2026-114
Preprint. Discussion started: 28 July 2026

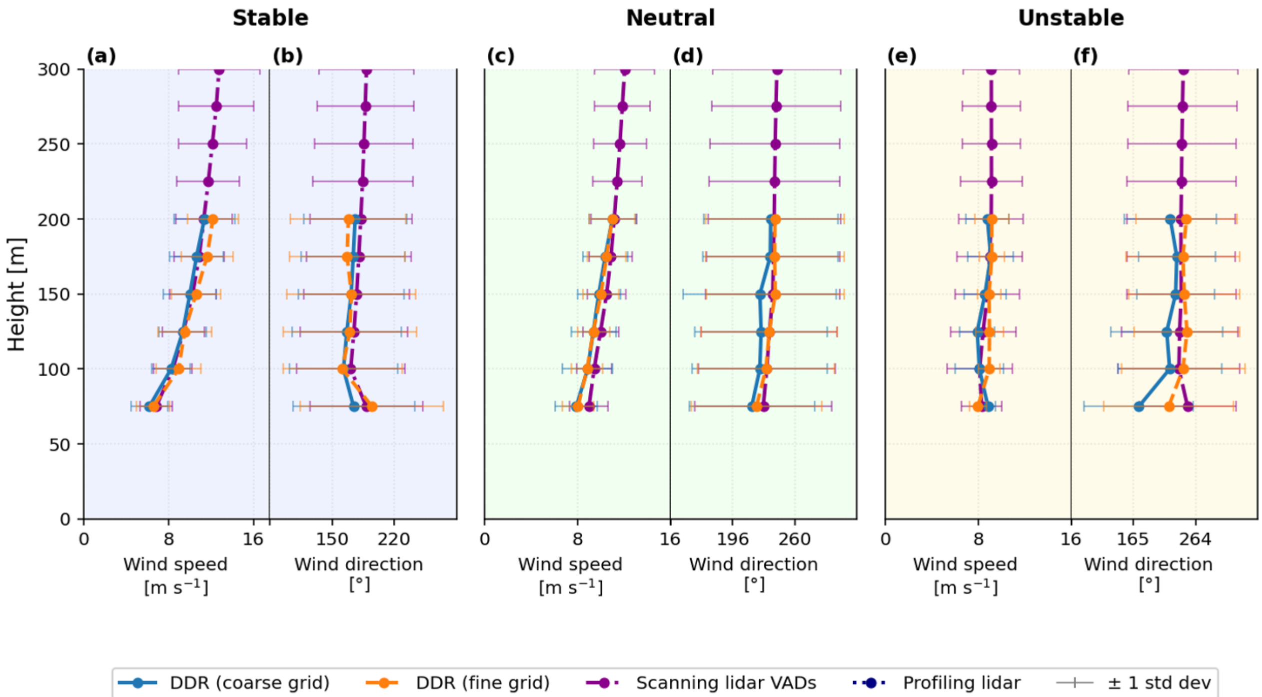

Figure 8. Ensemble-averaged profiles of wind speed and wind direction during the three stability regimes. The wind speed x-axis is the same across the three regimes, but the wind direction x-axis differs since flow direction changes based on stability.

narrower radar tilt angles applied, but the removal of influence supposedly generated by insects reduced this bias to the current results, which underscores both the effectiveness of the filtering and the need for its continued refinement.

Further insight on DDR performance can be explored in terms of sky coverage and precipitating conditions. An active German Weather Service station sat 29 km northeast of the WiValdi control center providing continuous measurements of cloud coverage and fog. As such, we desired to explore how the radar availability changes as a function of these different conditions. Cases were classified as foggy if visibility from the weather station measured less than 1000 m. All days with recorded rainfall intensity measurements from the disdrometer data were binned into the rain category regardless of cloud cover. As in Table 2, DDR data availability was measured by the fraction of available samples from the full DDR operating period, but lasting until the end of the year at 140 m, the height just above the wind turbine rotors.

Figure 9 depicts clear, partly cloudy, mostly cloudy, overcast without rain, rainy samples, and foggy samples in Figs. 9a-f, respectively. We separated these bins into the same warm (left) and cool (right) seasonal period used in the Figure 3 wind roses, ergo, the 'Rainy Conditions' category may also include snowfall. Across both seasons, the spatial distribution of radar data availability across the domain shows remarkably little sensitivity to non-precipitating sky coverage conditions. Under clear skies, partly cloudy, mostly cloudy, and overcast (no rain) conditions, the availability fraction patterns are broadly similar to one another for their respective season, with comparable spatial structures and no systematic change in data coverage as cloud

https://doi.org/10.5194/wes-2026-114
Preprint. Discussion started: 28 July 2026

eawe european academy of wind energy
Open Access WIND ENERGY SCIENCE DISCUSSIONS

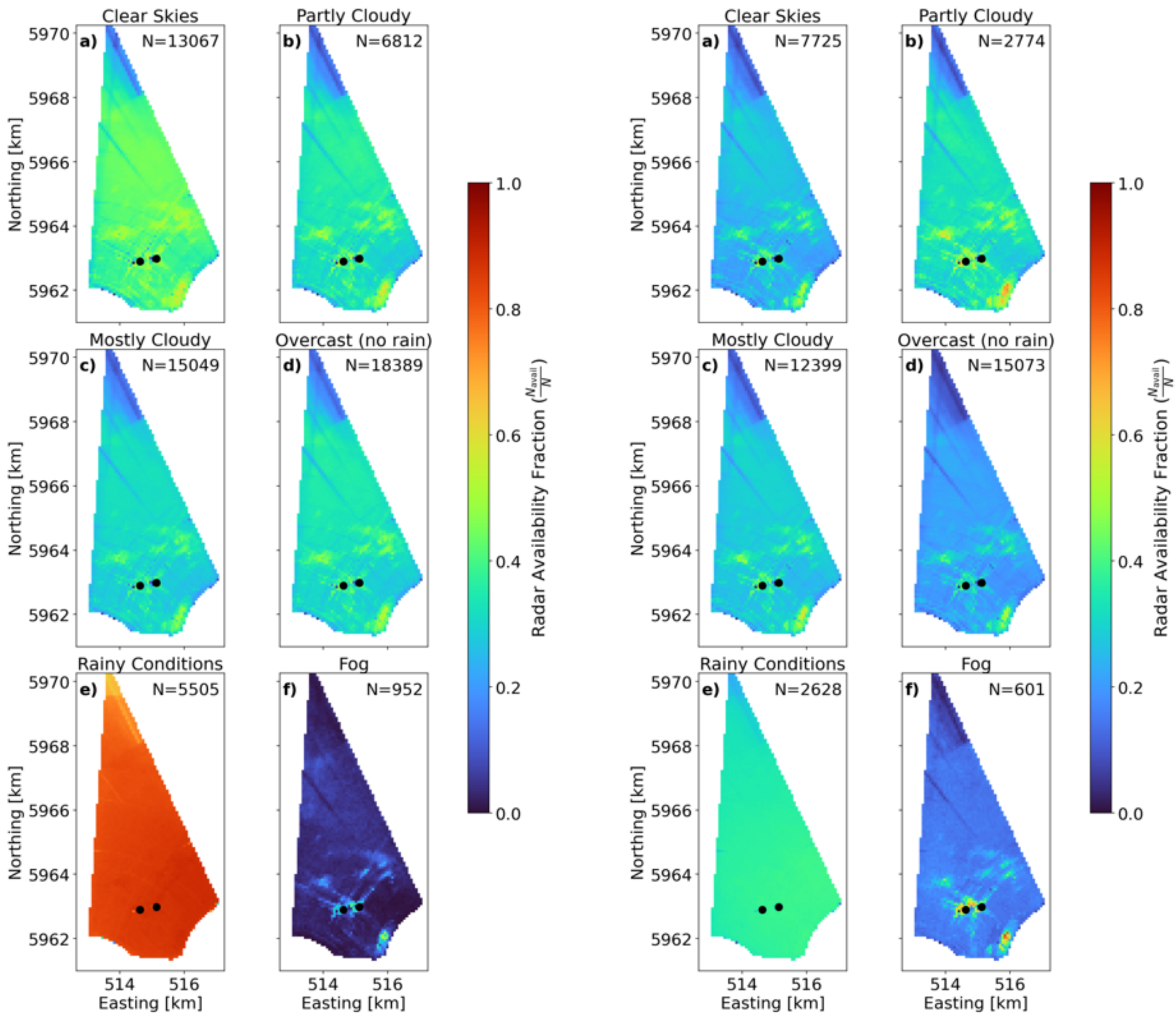

Figure 9. Seasonal spatial maps of DDR data availability fraction at 140 m across the WiValdi domain. Each is stratified by meteorological condition: (a) clear, (b) partly cloudy, (c) mostly cloudy, (d) overcast without rain, (e) rainy, and (f) foggy. The left grouping of these six plots represents the typical warm season (3 April-30 September 2025) while the right represents the cold season (1 October-31 December 2025). Availability is defined as the fraction of samples with valid DDR returns relative to the full operating period. Sky cover classifications are derived from a Deutscher Wetterdienst weather station located 29 km northeast of the WiValdi control center; foggy conditions are defined by visibility below 1000 m. All periods with recorded rainfall intensity from the onsite disdrometer are assigned to the rain category regardless of concurrent cloud cover.

https://doi.org/10.5194/wes-2026-114
Preprint. Discussion started: 28 July 2026

cover increases. During warm seasons, clear skies presented slightly stronger availability compared to other non-precipitating conditions, but this pattern was not reflected during cooler months. This indicates that the presence of clouds overhead, even a fully overcast sky, does not meaningfully improve or defer the radar's ability to retrieve wind measurements.

A pronounced shift in radar availability emerged under precipitating and foggy conditions, with both weather types producing availability patterns that diverged sharply from those observed under cloud-only regimes. During rainfall, the domain exhibited its highest and most spatially uniform availability across both periods. This result is particularly noteworthy given the comparatively modest sample sizes associated with rainy conditions, suggesting that precipitation itself actively enhances the density of valid radar returns. Foggy conditions, by contrast, resulted in a near-complete collapse of valid returns, with only isolated pockets of signal surviving across the domain. Seasonally, there were major differences in the actual fractional values: precipitating conditions in the colder months, foggy conditions yielded much higher levels of availability than warmer months, and vice-versa with precipitating conditions, reflecting the relevance of the types of hydrometeor droplets having an effect. Even so, this time period portrayed the same general pattern as the warmer months.

Altogether, these sky coverage results confirm that cloud conditions alone do not alone provide the scattering targets necessary for reliable retrieval performance. Rather, they confirm that it is a fundamental characteristic of X-band Doppler radar to require requires hydrometeors to act as scatterers and return a sufficiently strong signal. To this end, it is worth exploring if any precipitation specific measurements provide insight into DDR availability. In addition to rain intensity, the disdrometers provide measurements of raindrop number concentration and their kinetic energy when falling, offering further insight into the nature of the precipitating particles. As such, Figure 10 portrays the relationship between DDR data availability, where the rain particle number (Fig. 10a), the rain intensity used in Fig. 9 (Fig. 10b), and the kinetic energy of the droplets. Each of the axes spans the full range of observed precipitation rates on a logarithmic scale. the analysis is restricted to the DDR grid point collocated with the disdrometer location, which falls within the region of highest data availability during precipitation identified in Fig. 9.

Even at zero rain intensity, a non-negligible baseline availability of approximately 50% and 70% was observed (also seen in Figure 9), reflecting the radar's ability to detect aerosols, insects, or other clear-air targets under dry conditions. However, availability rose markedly and in a stepwise manner with increasing values across all three precipitation quantities shown in Figure 10. For particle count and rain intensity, notable jumps occurred around the 0.1 and 0.4 value thresholds, with availability climbing gradually thereafter. Kinetic energy exhibited the most distinct stepwise behavior of the three, with availability remaining near its baseline below the approximate value of 1 before rising sharply to near-complete coverage beyond that threshold, suggesting that drop size and fall velocity (both of which contribute to kinetic energy) may be more directly linked to radar scattering efficiency than intensity or count alone. Between particle count and rain intensity, the latter shows a slightly stronger relationship with DDR availability. However, none of the three quantities demonstrates a purely linear relationship with availability, and full domain coverage is rarely achieved even at high precipitation rates. This indicates that while DDR has a strong dependence on precipitation, other factors, such as droplet size distribution and the presence of biological scatterers, can prevent complete coverage even during active rain events.

https://doi.org/10.5194/wes-2026-114
Preprint. Discussion started: 28 July 2026

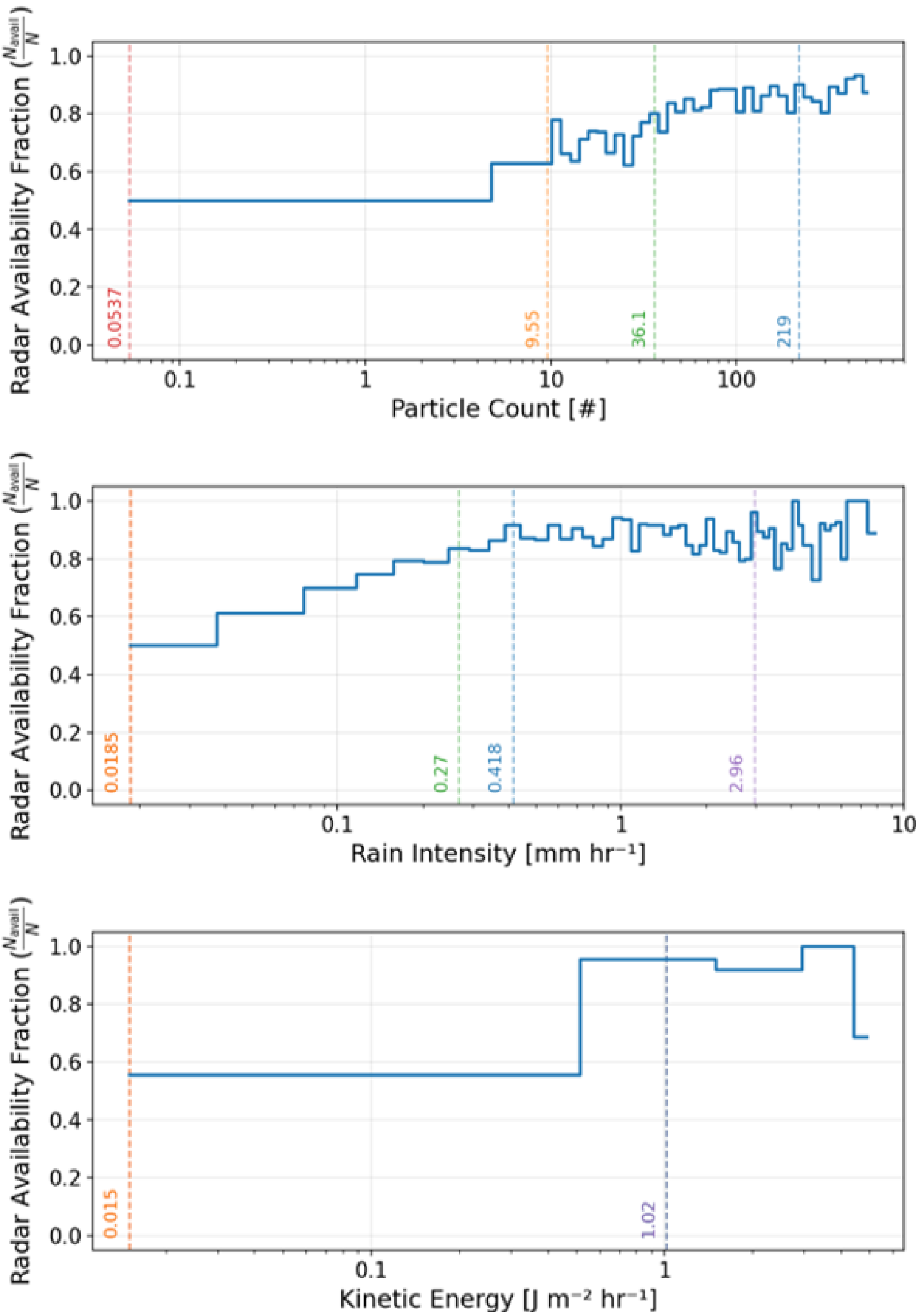

Figure 10. Logarithmic stepwise functions of precipitation droplet particle number (panel 10a), precipitation intensity (panel 10b), and kinetic energy of the droplets (panel 10c). The plot is representative of the full 3 April 2025 - 31 December 2025 period whenever DDR and precipitation occurred. The colored vertical lines were added in both panels to help denote the exact quantity thresholds for each variable. Only DDR coarse grid is shown as fine grid produced similar results.

https://doi.org/10.5194/wes-2026-114
Preprint. Discussion started: 28 July 2026

eawe european academy of wind energy
Open Access WIND ENERGY SCIENCE DISCUSSIONS

One particularly noteworthy component of the spatial availability results is that each condition scans except those during precipitation showed pockets of higher fraction values connected to artificial data. As of recently, an image processing method for DDR artifact removal was investigated in Zheng et al. (2026) and found to successfully remove radial streak effects caused by beam obstruction. However, the technique cannot differentiate between such artificial streaks and turbine wakes. Since the majority of artifacts closest to the turbines due to sidelobe contamination from turbine blockage, they must be considered when conducting wake analysis in and around turbines. Scans that present decent coverage without precipitation are most vulnerable to this contamination, so it recommended to target periods with enough precipitation that those effects are mitigated, or to focus on wind directions where wakes are not obstructed. One should also be mindful of the reduction in data availability with increasing distance from the radars, even under precipitating conditions. Vöhringer et al. (2024) found that wind speed agreement between DDR retrievals and profiling lidars degraded systematically with distance from the radar pair, suggesting that the Figure 9 reduced availability at greater ranges is an inherent characteristic of diminishing radar returns, showing spatial coverage in DDR wind retrievals can emerge at relatively close ranges depending on the scan strategy.

3.4 DDR Capabilities for Resolving Features in Flow Field

Beyond wind speed validation and assessment in different conditions, a key motivation for deploying DDR at Krummendeich was to explore its potential in resolving spatially coherent flow features and their evolution that are inaccessible to point measurement approaches, including LLJs. As discussed in Sect. 2.1, LLJs are a prominent feature of the nocturnal boundary layer at Krummendeich and are of direct relevance to wind energy given their role in producing pronounced wind shear at rotor-level heights. A multi-night LLJ episode in early June 2025 provided an opportunity to assess DDR performance in capturing this feature. Figure 11 presents time-height profiles of scanning lidar wind speed alongside MWR temperature and humidity over three consecutive nights. The lidar profiles in Fig. 11a show wind speed maximums indicative of the LLJ in the overnight hours, consistent with the decoupling of the nocturnal boundary layer under stable stratification. The MWR profiles in Fig. 11a and b corroborate this interpretation, where the LLJ nights were characterized by elevated temperatures and reduced moisture throughout the boundary layer relative to the preceding convective period. Based on supervisory control and data acquisition (SCADA) turbine monitoring records (Fig. 11d), only one turbine (the leftmost at the site) was shown to produce operational power during this period. We intended to view DDR scans before, during, and after LLJ formation (T1-T5) to determine if DDR winds also captured the jet. Not shown here is disdrometer data, as there was no precipitation during this 3-day period recorded.

Fine grid DDR scans from the five timestamps of T1–T5 are shown in Figure 12 at 90 m, 140 m, and 200 m. As a whole, the DDR successfully resolved the accelerated flow associated with the jet, with the elevated wind speeds visible in the horizontal wind fields at hub height and above during the LLJ timestamps. This was the case even regardless of the introduction of turbine-associated artifacts evident after T1 (Figs. 12a, f, and k), a time that managed to avoid the effects despite no precipitation. This helps to inform that there is a decent level of accuracy from the DDR winds that are measured, even when the coverage of those winds differs. Also, the spatial visualizations from T1 also insinuate both turbines were operational at a time when SCADA data from the rightmost turbine was not available in Fig. 11. Overall, this case shows the DDR method is capable of capturing

https://doi.org/10.5194/wes-2026-114
Preprint. Discussion started: 28 July 2026

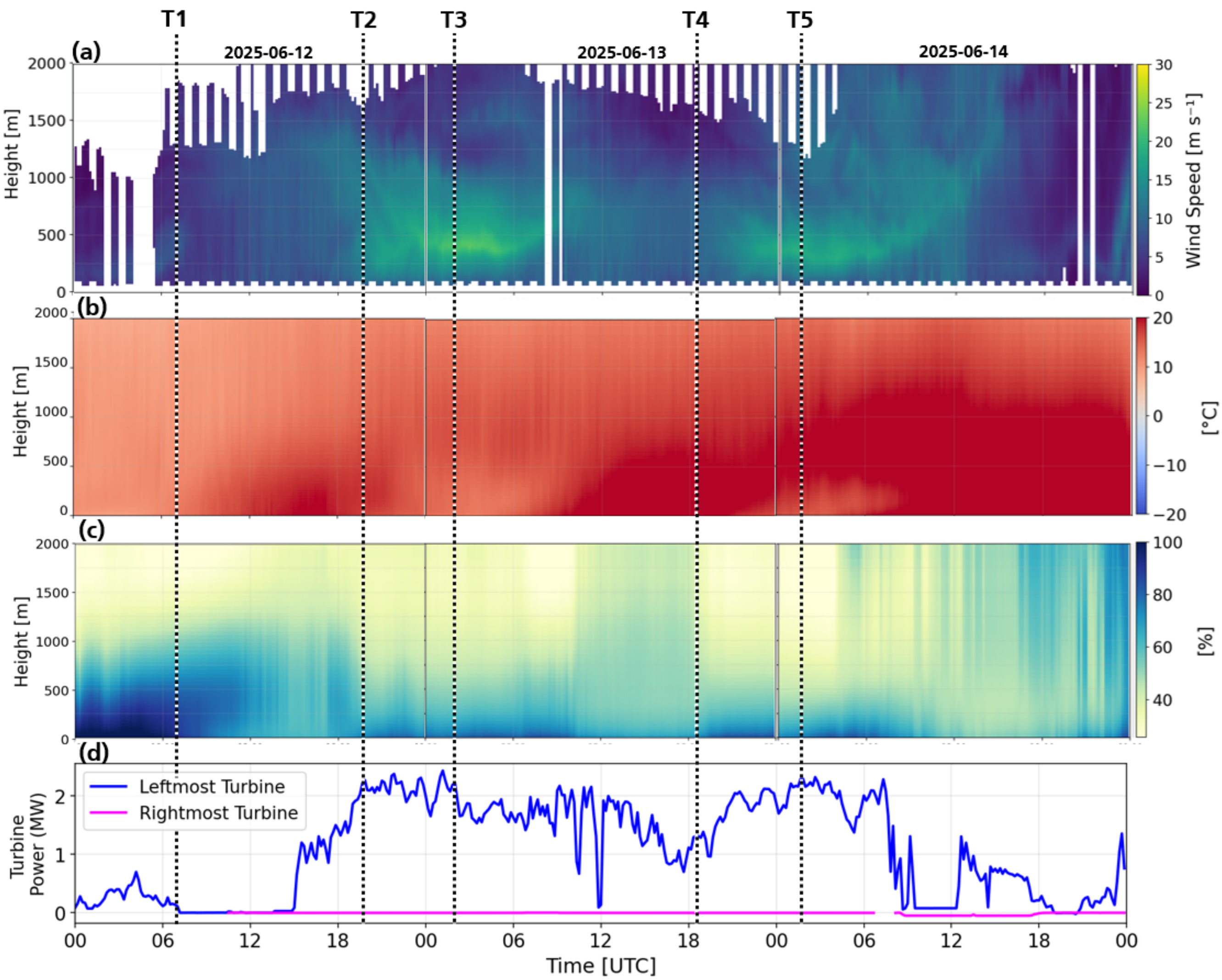

Figure 11. Time-height profiles of a multi-case period throughout which LLJs were identified overnight. Panels a, b, c, and d show scanning lidar wind speed, MWR temperature, MWR humidity, and turbine power outputs from supervisory control and data acquisition (SCADA) datasets. The vertical black dotted lines in the wind speed (black dotted lines in MWR profiles) denote five timestamps (T1–T5) throughout the period are denoted before, during, and after the LLJ.

https://doi.org/10.5194/wes-2026-114
Preprint. Discussion started: 28 July 2026

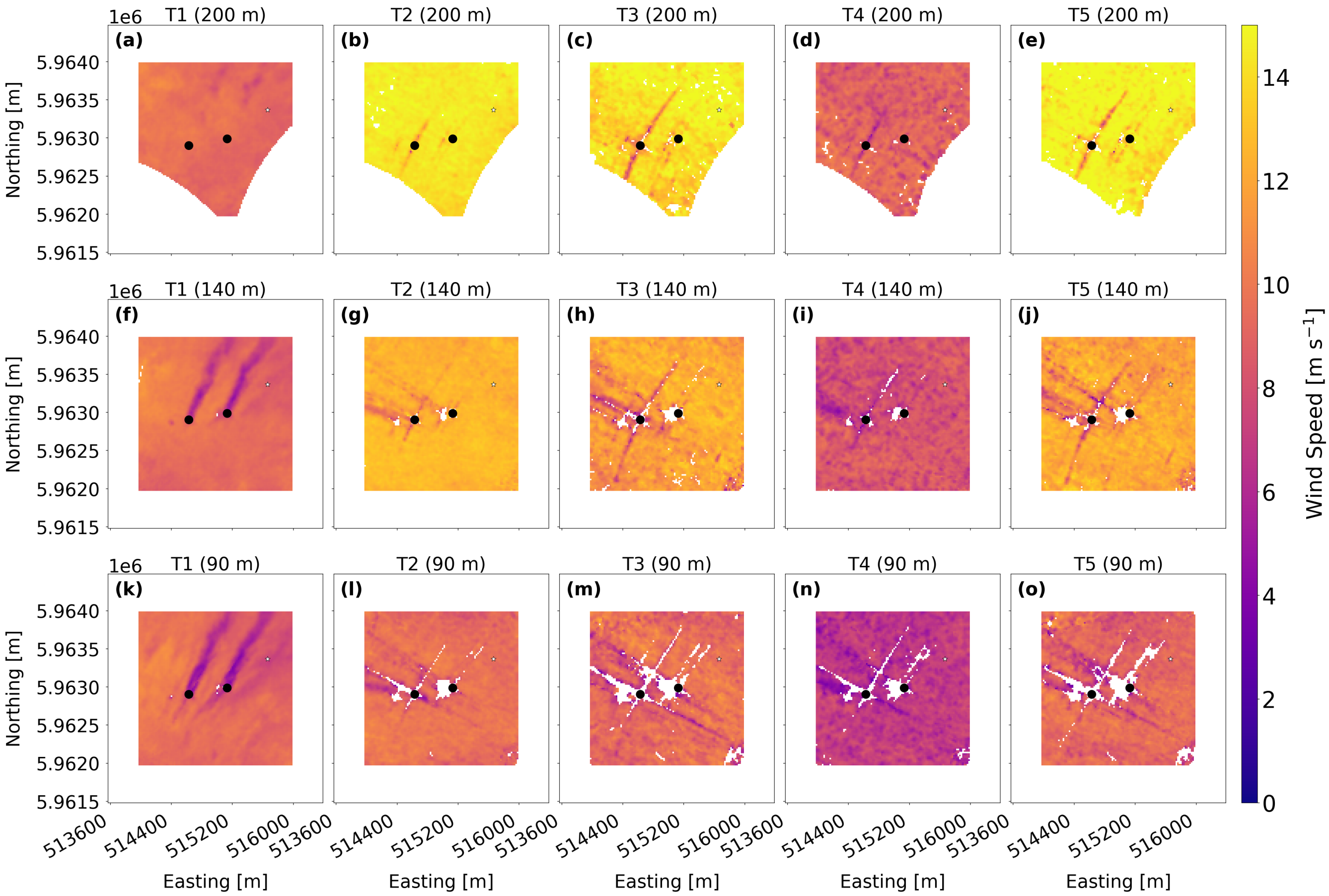

Figure 12. Fine grid DDR samples of scans over the June 6 - June 15, 2025 period. Each column corresponds to the T1-T5 timestamps in Figure 11, and each row shows scans at 200 m, 140 m, and 90 m, respectively.

mesoscale boundary layer structures beyond simple mean flow, representing an observational capability that complements the time-height perspective provided by the scanning lidar.

Given the sizable obstruction that can occur from turbine artifacts at hub-height, a common level for assessing wake effects using remote sensing instruments, there should be measures in place to avoid this contamination. For simple visualization purposes as done here, the artifacts may be eliminated at certain altitudes above the rotor disks, though this is strongly dependent on the case and Fig. 12 shows them to be especially present from the operating turbine even at the capping height of 200 m. Additionally, along-wake transects can be used to construct vertical cross-sections, though they be offset slightly laterally so that they run parallel to the turbine rather than through its center. Doing so avoids the near-field masking that would otherwise obscure the wake directly at the rotor location. With these considerations applied, Figure 13 presents three unique scans qualitatively illustrating distinct wake behaviors: a typical elongated single wake, wake interaction between turbines, and lateral wake meandering. For each case, we present a DDR fine grid spatial scan and stacked PPIs interpolated along the transect used

https://doi.org/10.5194/wes-2026-114
Preprint. Discussion started: 28 July 2026

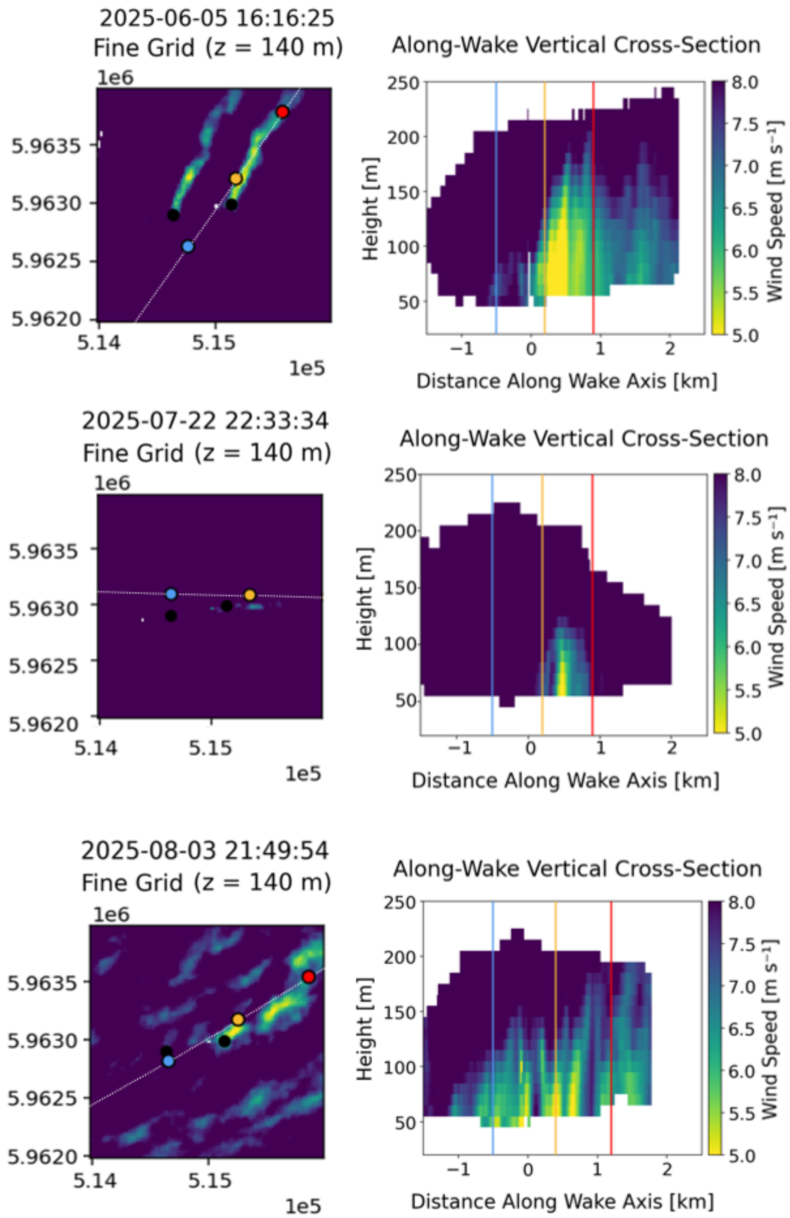

Figure 13. DDR scans of three different types of wake features: elongated wakes (first row), wake interaction (second row), and wake meandering (third row). The left column shows horizontal fine grid snapshots with transects draw (denoted by the dotted line and colored dots) while the right shows vertical cross-sections of the wake axes. The colored vertical lines correspond to the positioning of the colored dots in the horizontal view in the left column.

https://doi.org/10.5194/wes-2026-114
Preprint. Discussion started: 28 July 2026

to construct the vertical cross-sections shown in the right-hand panels. A transect was drawn at points along the wake that did not coincide with the areas of expected radar artifacts.

The top row (2025-06-06) shows a coherent wake signal extending several kilometers downwind under near-southerly flow, with the vertical cross-section revealing a well-defined velocity deficit concentrated below approximately 200 m and narrowing with downstream distance. The middle row (2025-07-23) captured wake interaction under near-westerly flow, which aligned both turbines nearly in the streamwise direction. The vertical cross-section revealed a more broadened and deepened velocity deficit at the downstream turbine location, reflecting the compounded momentum extraction that occurs when one turbine wake is ingested by a second. While such interactions were a dominant feature of the large-scale wind farms examined during AWAKEN (Moriarty et al., 2024), the present results demonstrate that DDR can efficiently resolve wake interaction signatures even within a two-turbine domain. The bottom row (2025-08-03) illustrates a case of strong lateral wake meandering, visible in the fine grid PPI as a sinuous deflection of the wake centerline. The vertical cross-section complements this horizontal view: rather than a monotonically decaying deficit, the wake oscillates and shifts laterally with height, a signature that would be entirely unresolvable with point measurements alone. Across all three cases, including the wake interaction where wake effects are the most diminished, the DDR method demonstrates a clear capability to resolve wake structure both spatially and vertically, capturing flow features that lie beyond the reach of conventional instrumentation even within a confined domain such as this. This matches findings from AWAKEN, while providing new insight of the method's ability to capture wake signals even from a couple turbines as opposed to large wind farms.

Still, the present study is merely interested in the capabilities of the method to capture such features whereas deeper, more intrinsic wake analysis is saved for future studies. It is expected that detailed wake analysis at hub-heights will be trickier with that being where turbine blockage artifacts are typically strongest, which Fig. 12 demonstrated. As mentioned, certain wind directions that avoid the bulk of the artifacts can be targeted (in the Fig. 12 example, but there is still filtering and signal processing methods to be explored, developed, and investigated for avoiding such contamination while still retaining data.

4 Discussion

The Krummendeich field experiment provided a well-instrumented, compact testbed for evaluating the DDR method in a small, temperate maritime domain. The location of the WiValdi wind farm offered interesting climatological occurrences characteristic of the broader North German coastal climate, and the campaign observations confirmed these to be well-represented during the period. Such conditions were also attractive for evaluating DDR as a proxy for wind measurement. Strong mid-latitude cyclones frequently delivered precipitation that helped sustain DDR availability, and the method could be examined across different stability conditions strongly governed by wind direction.

Validation of the DDR against collocated scanning lidar ouputs showed notable agreement across most height levels. This was true particularly in the DDR fine grid, in which the compact domain geometry permitted reliable retrievals at lower altitudes than were achievable at AWAKEN, where large scan spacing amplified near-surface uncertainties. As a whole, overestimation in DDR samples were very limited or non-existent compared to AWAKEN. In that campaign, large-scale DDR measurements presented a high wind speed bias concentrated near the surface, attributed to surface roughness or residual grid interpolation effects from removing ground clutter. The processed DDR runs at Krummendeich did not present this bias owing to the use of narrower scan sectors. However, the scans did present strong overestimation near 10% prior to the filtering of biological scatterers, showing the necessity of considering bugs and birds in DDR, even in small, confined coverage domains.

No systematic degradation in DDR performance was observed across the stability regimes encountered during the campaign, showing that the method transfers well across the range of atmospheric conditions typical of this temperate coastal environment. In particular, we found that data availability was much more strongly connected to hydrometeors than sky cover. Precipitating samples yielded strong domain coverage, especially closer to the radar. The only instance clouds strongly impacted DDR were foggy conditions, which significantly inhibited the amount of valid returns. The analysis further deduced how DDR availability is tied to the particle number of droplets and the intensity of precipitation, where intensity showed slightly higher proportionality. Further insight on types of hydrometeors (e.g., rain, snow, hail) would largely benefit applications of DDR and its application to regions where one or the other is more prominent.

Finally, the DDR method demonstrated a clear capability for resolving features in the wind flow, such as nocturnal LLJs and different types of turbine wake signatures. Despite originating from single turbines rather than the collective wakes of large wind farms as in AWAKEN, the DDR method efficiently captured wake evolution; this represents spatial information that is inaccessible to point measurement approaches even within a two-turbine domain. Near-field turbine blockage, where the rotor structure obscures radar returns directly behind the hub, remains a persistent practical constraint but can be mitigated through transect offsetting or elevated height selection, keeping in mind that direct near-wake access remains constrained.

As with all measurement techniques, the DDR method carries its own limitations. Since the radar beam has an opening angle of 0.5°, the probe volume increases with range. In addition, the Cartesian gridded wind vectors are obtained using an objective analysis with a radius of influence (ROI) that increases with distance from the radar pair. As a result, grid points at larger ranges represent averages over larger atmospheric volumes than grid points closer to the radars. At the same time, data availability typically decreases with range, so that these larger volumes are often sampled by fewer independent measurements, which may further affect the uncertainty of the wind retrievals. Another consideration is that the temporal resolution of dual-Doppler scans is inherently constrained by the time required for both radars to complete coordinated volume scans, meaning that rapidly evolving flow features may not always be fully captured between successive syntheses. A major drawback routinely seen here is how radar artifacts can compromise otherwise suitable observations, ranging from biological scatterers to turbine sidelobe contamination, and the processing and filtering measures applied here may not translate directly to all DDR configurations or deployment geometries. Though this is nothing new pertaining to radar technology in general, it warrants particular consideration for analyzing waked flow. Further, the DDR method is that strong data availability requires substantial hydrometers for the radar beams to scatter off. This means the quantity of the DDR scans themselves become comprised except where precipitation is climatologically common and can otherwise struggle to provide statistical measures. Even so, DDR cases that present good availability without precipitation are possible, as the Fig. 11 case study revealed. Returns like these present more opportunities for DDR-lidar comparisons that are otherwise limited since the lidar signal usually becomes extinct in heavy precipitation. Further, if statistical information is limited, DDR case studies remain valuable for many applications in

https://doi.org/10.5194/wes-2026-114
Preprint. Discussion started: 28 July 2026

the industry and beyond, and the case studies herein addressed a major objective of the Krummendeich campaign: to confirm that DDR is capable of resolving spatially coherent flow features that lie beyond the reach of point measurement approaches.

5 Conclusions

The Krummendeich campaign was a vital resource in studying the DDR method and its capabilities. The DDR data proved to be a viable wind measurement tool across the range of conditions that were typical of a temperate maritime coastal environment. We found that the DDR winds matched those from the lidar well, with only minor disagreement at lower levels. Data availability was governed primarily by hydrometeor presence, with precipitation yielding near-complete domain coverage and fog causing near-total signal loss. Lastly, the spatial ranges offered by DDR resolved different characteristics from the flow field with height and horizontal distance, bearing in mind that data especially around the turbines could be obstructed due to blockage.

This study intended to focus on general DDR performance during the Krummendeich campaign, but there are many plans in place for upcoming analysis in future studies. One strong avenue for investigation being quantifying turbulence information from radar scans. This has been achieved using specific methods in Gunter et al. (2015) and Hirth et al. (2020), but analyzing the accuracy of such techniques in wind energy campaigns provided by Krummendeich or AWAKEN has not yet been accomplished. Plans are underway to enact similar methods to both campaigns, which can further be assessed in another offshore campaign implementing DDR planned for 2026. Data from the offshore campaign will provide an added gateway into more data in another location, allowing for more analysis into other topics discussed here necessitating further analysis, such as cold season comparisons, how turbine-induced contamination enters the radar sidelobes as a function of turbine size, orientation, and layout, and how such contamination can be mitigated or systematically flagged during data analysis.

Code availability. Python scripts used to produce the plots used in this paper are available upon request.

Appendix A: Profiling and Scanning Lidar Comparisons

Different instruments operating throughout the Krummendeich field experiment were cross-validated against one another to understand how each captured the flow field and to establish confidence in their use as reference datasets. Of particular relevance here, the scanning lidar was validated against the co-located vertical profiling lidar prior to its use as the primary DDR reference, given the profiling lidar's well-established performance characteristics at this site. These comparisons were carried out at multiple height levels for both the 35° and 75° VAD configurations, with results shown in Figure A1. Although the rain-exclusion filtering reduced the total number of available data pairs relative to the full campaign record, the remaining comparisons demonstrate strong agreement across all examined levels, supporting the use of the scanning lidar as a robust and reliable reference against which the DDR retrievals are subsequently evaluated.

https://doi.org/10.5194/wes-2026-114
Preprint. Discussion started: 28 July 2026

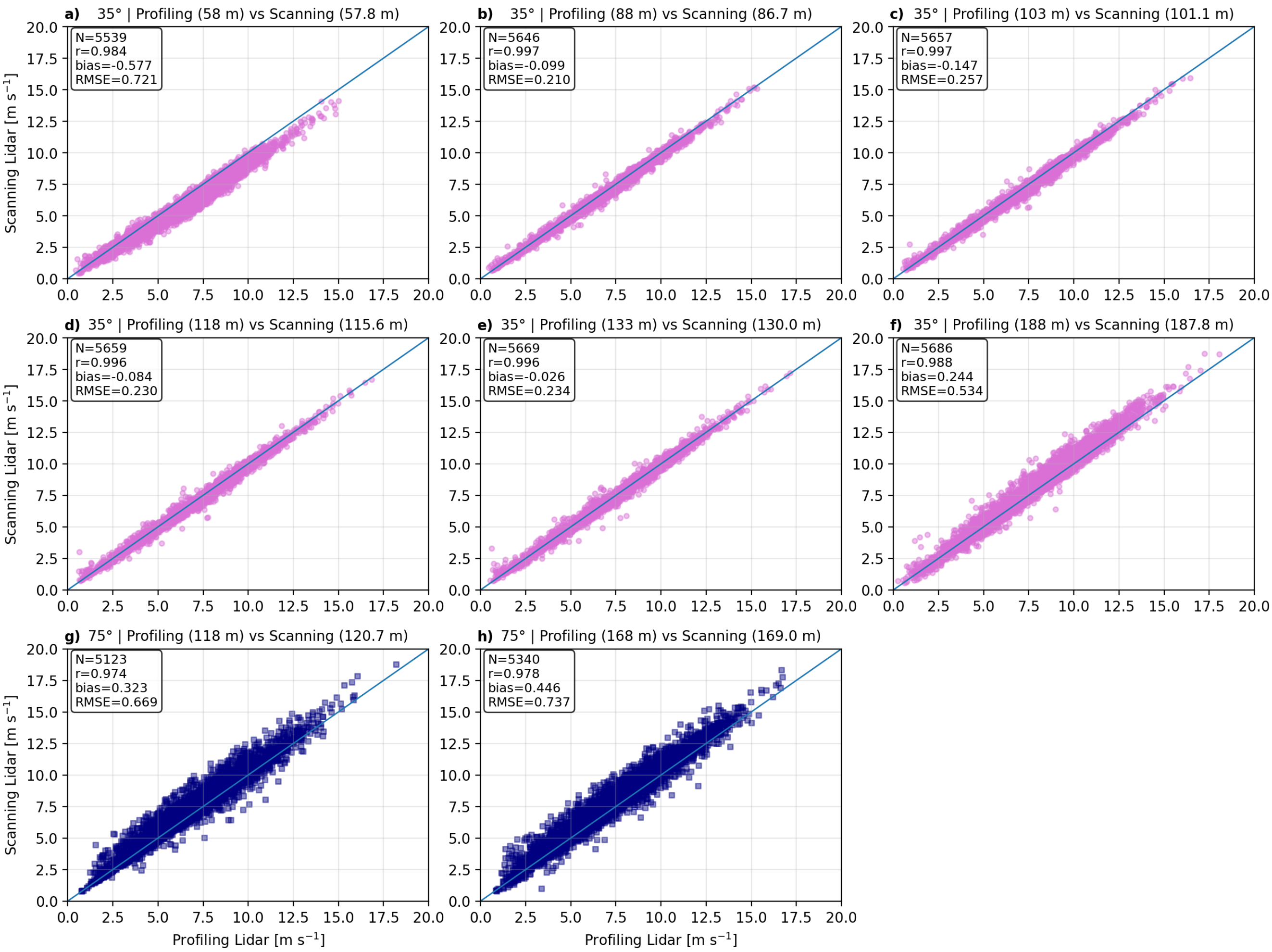

Figure A1. Correlation plots between the co-located vertical profiling lidar and IWES scanning lidar at roughly 58, 88, 103, 118, 133, and 188 m from 35° (panels a-f, respectively) and 118 and 168 m from the 75° (panels g-h, respectively).

https://doi.org/10.5194/wes-2026-114
Preprint. Discussion started: 28 July 2026

At the 35° elevation angle, agreement between the two lidar systems is generally strong at and above hub height. At the lowest elevation levels, however, the scanning lidar is subject to a blind zone arising from the finite distance between the instrument and the region where the cone of beam intersections first reaches the measurement height. Within this blind zone, the scanning lidar cannot resolve the wind field reliably, leading to erroneous wind speed estimates at the lowest levels visible in A1a. Retrievals recover well approaching hub height, as shown in Fig. A1b-f, once the beam geometry provides sufficient measurement geometry for accurate wind vector reconstruction.

A similar blind zone effect was apparent in comparisons at the 75° elevation angle in Fig. A1g-h. Because the steeper cone exhibits a narrower horizontal footprint, the blind zone extends to comparatively higher levels than at 35°, resulting in greater disagreement between the profiling and scanning lidars in the lowest portion of the profile. The number of height levels available for comparison at 75° is also more limited owing to the coarser vertical spacing inherent to the steeper scan geometry. Nevertheless, the strong agreement observed at the 35° elevation angle, combined with the physically consistent behavior at 75°, demonstrates that the scanning lidar performs systematically and as expected across both configurations. This establishes confidence in its use as a reference dataset against which the dual-Doppler radar retrievals are subsequently evaluated.

Proceeding to comparisons between the scanning lidar and DDR, Fig. 7 using the same elevation angles as in Fig. A1, overall agreement is strong across most height levels, with Pearson correlation coefficients ranging from r=0.872 to r=0.944 across all panels. However, there were systematic biases, especially at the same levels discrepancies were highest from Fig. A1, showing the blind zone effect here as well. At the heights in Fig. 7, the scanning lidar was seen to measure well, the were well aligned with r between 0.93 and 0.95, insinuating adequate performance from the considering differences in instrument scanning capabilities and range coverage.

Note that the rain-exclusion filter applied in the profiling–scanning lidar comparisons of is intentionally not applied here, as characterizing DDR performance under precipitating conditions is a central objective of this study. During precipitation events, hydrometeors can bias scanning lidar-derived wind speed estimates from the scanning lidar by enhancing backscatter and partially attenuating the beam, which likely contributes to the scatter visible at lower wind speeds in several panels. This means that some of the residual disagreement between the scanning lidar and DDR at lower levels reflects scanning lidar errors rather than DDR errors, reinforcing the conclusion that the scanning lidar serves as a reliable reference primarily above the blind zone and outside of heavy precipitation periods.

A1

Author contributions. AMJ wrote the original draft and post-processed the scanning lidar data. Both LH and GW post-processed the dual-Doppler radar data and provided underlying guidance to the working with the files. JG edited and provided corrections. All authors reviewed this paper.

Competing interests. At least one of the (co-)authors is a member of the editorial board of Wind Energy Science.

https://doi.org/10.5194/wes-2026-114
Preprint. Discussion started: 28 July 2026

Acknowledgements. The presented research was conducted as part of the Windpark RADAR project for the validation and demonstration of dual-Doppler radar measurements, funded by the Federal Ministry for Economic Affairs and Energy (BMWE) under grant number 03EE3031A, as well as the support of Project Management Jülich (PTJ). The measurement was conducted on the wind energy research farm WiValdi at its Krummendeich site in Lower Saxony developed and operated by the Deutsches Zentrum für Luft- und Raumfahrt (DLR), and the Lower Saxony Ministry of Science and Culture (MWK). We wish to also acknowledge SmartWind Technologies for their support and discussion in assessing the dual-Doppler radar products. Finally, we acknowledge the utilization of generative AI tools for assistance with manuscript preparation.

https://doi.org/10.5194/wes-2026-114
Preprint. Discussion started: 28 July 2026

References

Abraham, A., Hamilton, N., Bodini, N., Hirth, B., Schroeder, J., Letizia, S., Krishnamurthy, R., Newsom, R., and Moriarty, P.: Land-based wind plant wake characterization using dual-Doppler radar measurements at AWAKEN, J. Phys.: Conf. Ser., 2767, 092 037, https://doi.org/10.1088/1742-6596/2767/9/092037, 2024.

Ahsbahs, T., Nygaard, N. G., Newcombe, A., and Badger, M.: Wind farm wakes from SAR and Doppler radar, Remote Sens., 12, 462, https://doi.org/10.3390/rs12030462, 2020.

Bingöl, F., Mann, J., and Larsen, G. C.: Light detection and ranging measurements of wake dynamics part I: one-dimensional scanning, Wind Energy, 13, 51–61, https://doi.org/10.1002/we.352, 2010.

Bluestein, H. et al.: Radar in Atmospheric Sciences and Related Research: Current Systems, Emerging Technology, and Future Needs, Bull. Am. Meteorol. Soc., 95, 1850–1861, https://doi.org/10.1175/BAMS-D-12-00241.1, 2014.

Christiansen, M. B. and Hasager, C. B.: Wake effects of large offshore wind farms identified from satellite SAR, Remote Sens. Environ., 98, 251–268, https://doi.org/10.1016/j.rse.2005.07.009, 2005.

Clifton, A., Clive, P., Gottschall, J., Schlipf, D., Simley, E., Simmons, L., Stein, D., Trabucchi, D., Vasiljevic, N., and Würth, I.: IEA Wind Task 32: Wind lidar identifying and mitigating barriers to the adoption of wind lidar, Remote Sens., 10, 406, https://doi.org/10.3390/rs10030406, 2018.

Emeis, S., Siedersleben, S., Lampert, A., Platis, A., Bange, J., Djath, B., Schulz-Stellenfleth, J., and Neumann, T.: Exploring the wakes of large offshore wind farms, J. Phys.: Conf. Ser., 753, 092 014, https://doi.org/10.1088/1742-6596/753/9/092014, 2016.

Given, T. and Ray, P. S.: Response of a two-dimensional dual-Doppler radar wind synthesis, J. Atmos. Oceanic Technol., 11, 239–255, 1994.

Gottschall, J.: Wake Measurements with Lidar, https://doi.org/10.1007/978-3-030-31307-4_55, 2022.

Gottschall, J., Papetta, A., Kassem, H., Meyer, P. J., Schrempf, L., Wetzel, C., and Becker, J.: Advancing wind resource assessment in complex terrain with scanning lidar measurements, Energies, 14, 3280, https://doi.org/10.3390/en14113280, 2021.

Gunter, W. S., Schroeder, J. L., and Hirth, B. D.: Validation of Dual-Doppler Wind Profiles with In Situ Anemometry, J. Atmos. and Ocean. Tech., 32, 943–960, https://doi.org/10.1175/JTECH-D-14-00181.1, 2015.

Hasager, C. B., Vincent, P., Husson, R., Mouche, A., Badger, M., Peña, A., Volker, P., Badger, J., Di Bella, A., Palomares, A., Perez, B., and Correia, O.: Using satellite SAR to characterize the wind flow around offshore wind farms, Energies, 8, 5413–5439, https://doi.org/10.3390/en8065413, 2015.

Hirth, B. D. and Schroeder, J. L.: Documenting wind speed and power deficits behind a utility-scale wind turbine, J. Appl. Meteorol. Climatol., 52, 39–46, https://doi.org/10.1175/JAMC-D-12-0145.1, 2013.

Hirth, B. D., Duncan, J. B., and Schroeder, J. L.: Characterizing Turbine Inflow during a Stability Transition using Dual-Doppler Radar Measurements, J. Phys.: Conf. Ser., 1618, 032 030, https://doi.org/10.1088/1742-6596/1618/3/032030, 2020.

Hung, L. and Gottschall, J.: Assessment of position accuracy for scanning dual-Doppler X-band wind radar systems, J. Phys.: Conf. Ser., 3224, 022 058, https://doi.org/10.1088/1742-6596/3224/2/022058, 2026.

Hung, L.-Y., Gottschall, J., Lilén Vöhringer, A., Hirth, B. D., and Schroeder, J. L.: Comparison of line-of-sight wind speed measurements from an X-band radar and a long-range scanning lidar, J. Phys.: Conf. Ser., 2767, 042 030, https://doi.org/10.1088/1742-6596/2767/4/042030, 2024.

Iungo, G. V., Wu, Y.-T., and Porté-Agel, F.: Field measurements of wind turbine wakes with lidars, J. Atmos. Oceanic Technol., 30, 274–287, https://doi.org/10.1175/JTECH-D-12-00051.1, 2013.

https://doi.org/10.5194/wes-2026-114
Preprint. Discussion started: 28 July 2026

Lampert, A., Cañadillas, B., Rausch, T., Schmitt, L., Djath, B., Schulz-Stellenfleth, J., Platis, A., zum Berge, K., Schäfer, I., Bange, J., Neumann, T., Dörenkämper, M., Stoevesandt, B., Gottschall, J., Vollmer, L., Emeis, S., Barekzai, M., Siedersleben, S., Kühn, M., Steinfeld, G., Heinemann, D., Peinke, J., Heißelmann, H., Schneemann, J., Centurelli, G., Waldmann, P., and Bärfuss, K.: Airborne measurements for investigating offshore wind farm wakes and modifications of sea state – benefits and limitations, Wind Energy Sci. Discuss., https://doi.org/10.5194/wes-2025-277, in review, 2026.

Lhermitte, R. M. and Gilet, M.: Dual-Doppler radar observation and study of sea breeze convective storm development, J. Appl. Meteorol. Climatol., 14, 1346–1361, https://doi.org/10.1175/1520-0450(1975)014<1346:DDROAS>2.0.CO;2, 1975.

Li, X., Chi, L., Chen, X., Ren, Y., and Lehner, S.: SAR observation and numerical modeling of tidal current wakes at the East China Sea offshore wind farm, J. Geophys. Res. Oceans, 119, 4958–4971, https://doi.org/10.1002/2014JC009822, 2014.

Louis, J.-F.: A parametric model of vertical eddy fluxes in the atmosphere, Boundary-Layer Meteorol., 17, 187–202, https://doi.org/10.1007/BF00117978, 1979.

Moriarty, P., Hamilton, N., Debnath, M., Herges, T., Isom, B., Lundquist, J. K., Maniaci, D., Naughton, B., Pauly, R., Roadman, J., Shaw, W., van Dam, J., and Wharton, S.: American WAKE experimeNt (AWAKEN), Tech. rep., National Renewable Energy Laboratory (NREL), Golden, CO (United States), https://doi.org/10.2172/1659798, 2020.

Moriarty, P., Bodini, N., Letizia, S., Abraham, A., Ashley, T., Bärfuss, K. B., Barthelmie, R. J., Brewer, A., Brugger, P., Feuerle, T., Frère, A., Goldberger, L., Gottschall, J., Hamilton, N., Herges, T., Hirth, B., Hung, L.-Y. L., Iungo, G. V., Ivanov, H., Kaul, C., Kern, S., Klein, P., Krishnamurthy, R., Lampert, A., Lundquist, J. K., Morris, V. R., Newsom, R., Pekour, M., Pichugina, Y., Porté-Angel, F., Pryor, S. C., Scholbrock, A., Schroeder, J., Shartzer, S., Simley, E., Vöhringer, L., Wharton, S., and Zalkind, D.: Overview of preparation for the American WAKE ExperimeNt (AWAKEN), J. Renew. and Sus. Energy, 16, https://doi.org/10.1063/5.0141683, 2024.

Nygaard, N. G. and Newcombe, A. C.: Wake behind an offshore wind farm observed with dual-Doppler radars, J. Phys.: Conf. Ser., 1037, 072 008, https://doi.org/10.1088/1742-6596/1037/7/072008, 2018.

Patel, A., Syed, A. H., Hung, L.-Y., and Mann, J.: Lidar observations of turbulence for tall offshore wind turbines, J. Flu. Mech., https://doi.org/10.1017/jfm.2025.111038, 2025.

Peel, M. C., Finlayson, B. L., and McMahon, T. A.: Updated world map of the Köppen-Geiger climate classification, Hydrol. Earth Syst. Sci., 11, 1633–1644, https://doi.org/10.5194/hess-11-1633-2007, 2007.

Platis, A., Siedersleben, S. K., Bange, J., Lampert, A., Bärfuss, K., Hankers, R., Cañadillas, B., Foreman, R., Bange, J., Kühn, M., Emeis, S., and Hasager, C.: First in situ evidence of wakes in the far field behind offshore wind farms, Sci. Rep., 8, 2163, https://doi.org/10.1038/s41598-018-20389-y, 2018.

Platis, A., Hundhausen, M., Lampert, A., Emeis, S., and Bange, J.: The Role of Atmospheric Stability and Turbulence in Offshore Wind-Farm Wakes in the German Bight, Bound.-Lay. Meteorol., 182, 441–469, https://doi.org/10.1007/s10546-021-00668-4, 2022.

Trujillo, J.-J., Bingöl, F., Larsen, G. C., Mann, J., and Kühn, M.: Light detection and ranging measurements of wake dynamics. Part II: two-dimensional scanning, Wind Energy, 14, 61–75, https://doi.org/10.1002/we.402, 2011.

Vöhringer, A. L., Gottschall, J., Hirth, B. D., Hung, L.-Y., Lundquist, J. K., Schneemann, J., Schroeder, J. L., Theuer, F., and Kühn, M.: Comparison of horizontal wind speed and direction measurements from dual-Doppler radar and profiling lidars, J. Phys.: Conf. Ser., 2767, 092 101, https://doi.org/10.1088/1742-6596/2767/9/092101, 2024.

Wildmann, N., Hagen, M., and Gerz, T.: Enhanced resource assessment and atmospheric monitoring of the research wind farm WiValdi, J. Phys.: Conf. Ser., p. 022029, 2022.

https://doi.org/10.5194/wes-2026-114
Preprint. Discussion started: 28 July 2026

Wildmann, N., Thayer, J. D., Detring, C., and Päschke, E.: Gust-detection from velocity azimuth display Doppler wind lidar profiling at the WiValdi research park, J. Phys.: Conf. Ser., 2767, 092 076, https://doi.org/10.1088/1742-6596/2767/9/092076, 2024.

Zheng, Q., Hung, L., Jordan, A., and Gottschall, J.: An Extensive Framework for Preparing Dual-Doppler Radar Measurements for Wake Model Validation: Application to the AWAKEN Large-scale Field Experiment, J. of Renew. and Sus. Energy, 18, 043 302, https://doi.org/10.1063/5.0331761, 2026.

Zhou, L., Kulls, C., and Kisi, O.: Unveiling precipitation patterns in Schleswig-Holstein: a 50-year study of trends and climatic influences, Stoch. Environ. Res. Risk Assess., https://doi.org/10.1007/s00477-025-03087-w, 2025.